

Robust training of implicit generative models for multivariate and heavy-tailed distributions with an invariant statistical loss

José Manuel de Frutos^{a,*}

JOFRUTOS@ING.UC3M.ES

Manuel A. Vázquez^a

MAVAZQUE@ING.UC3M.ES

Pablo M. Olmos^a

PAMARTIN@ING.UC3M.ES

Joaquín Míguez^a

JMIGUEZ@ING.UC3M.ES

^aDepartment of Signal Theory and Communications, Carlos III University of Madrid, Leganés 28911, Madrid, Spain

Abstract

Traditional implicit generative models rely on adversarial discriminators, which can lead to unstable optimization and mode collapse. In contrast, the *Invariant Statistical Loss* (ISL) framework (de Frutos et al., 2024) defines a divergence between real and generated distributions by comparing empirical ranks. We provide a formal characterization of ISL as a proper divergence on continuous distributions, and prove that it is both continuous and differentiable, making it suitable for gradient-based training without adversarial instability.

To broaden ISL’s applicability, we address two key limitations. Many real-world distributions exhibit heavy tails that standard Gaussian-based generators fail to capture. We introduce Pareto-ISL, replacing the latent Gaussian noise with a generalized Pareto distribution, enabling the generator to better represent both central and extreme events. We also extend ISL to multivariate data through ISL-slicing, a scalable approach that projects data onto random one-dimensional subspaces, computes rank-based losses per slice, and averages them. This preserves joint structure while remaining computationally efficient.

Together, these contributions make ISL a practical and robust objective across a range of settings. In experiments, Pareto-ISL improves tail fidelity, and ISL-slicing scales effectively to high-dimensional data while also serving as a strong pretraining strategy for GANs.

Keywords: implicit generative models, deep generative models, mode collapse, heavy-tailed distributions, multivariate distributions

1 Introduction

1.1 Motivation

Generative modeling lies at the heart of many machine-learning applications—from density estimation (Kingma et al., 2013; Ho et al., 2020; Papamakarios et al., 2021) and data augmentation (Shorten and Khoshgoftaar, 2019) to unsupervised representation learning (Radford et al., 2015; Chen et al., 2016). Broadly speaking, these models fall into two categories (see Mohamed and Lakshminarayanan (2016)): *prescribed models*, which posit and optimize an explicit density (e.g., variational autoencoders (Kingma et al., 2013) or diffusion-based models (Ho et al., 2020)), and *implicit models*, which learn to generate samples by transforming simple latent noise through a neural network, without ever evaluating a tractable likelihood, for example, generative adversarial networks (GANs).

*. Corresponding author.

Since the seminal introduction of GANs by Goodfellow et al. (2014), implicit generative modeling has become a cornerstone of modern unsupervised learning. GANs define a two-player minimax game between a generator, which transforms latent noise into samples, and a discriminator, which learns to distinguish real from generated data. While they are capable of producing sharp and high-fidelity outputs, early GANs were plagued by training instability and *mode collapse*, where the generator fails to capture the full diversity of the data distribution (see Arora et al. (2018)).

To address these issues, a wide range of architectural and theoretical strategies have been developed. The Wasserstein GAN (WGAN) (Arjovsky et al., 2017) replaces the Jensen–Shannon divergence with the Earth Mover’s distance, resulting in more stable gradients and training dynamics. This requires enforcing Lipschitz continuity on the discriminator—initially via weight clipping and later improved with gradient penalties (Gulrajani et al., 2017). Spectral normalization (Miyato et al., 2018), unrolled optimization (Metz et al., 2016), and Jacobian regularization (Mescheder et al., 2018) can be used to improve convergence and reduce oscillatory behavior. Multi-discriminator setups (Durugkar et al., 2016; Choi and Han, 2022) and kernel-based alternatives like MMD-GAN (Li et al., 2017) and Cramér GAN (Bellemare et al., 2017) have also been explored to address mode collapse. At the architectural level, models such as BigGAN (Brock et al., 2018) and StyleGAN (Karras et al., 2019, 2020, 2021) introduce progressive growing, adaptive normalization, and class conditioning to improve sample quality and control.

While these advances improve training stability and sample realism, they primarily focus on distributions with bounded or light-tailed support. A few recent efforts have begun to tackle the problem of modeling heavy-tailed distributions. For example, ExGAN (Bhatia et al., 2021) introduces a tail-adaptive training objective to emphasize rare, high-magnitude samples. Pareto GAN (Huster et al., 2021) modifies the latent space by injecting non-Gaussian, Pareto-distributed noise to better capture extreme-value behavior. However, these models continue to rely on adversarial training, which becomes even more fragile in heavy-tailed settings and requires careful tuning and regularization.

Despite these advances, GAN training remains highly sensitive to hyperparameters and often requires heuristic stabilization techniques. Moreover, implicit models frequently struggle to capture extreme events and heavy-tailed behaviors—phenomena that are especially important in domains such as finance, climate modeling, and anomaly detection (Lu et al., 2023; Gong et al., 2024; Seo et al., 2024).

To address these issues, we build on the *Invariant Statistical Loss* (ISL) framework of de Frutos et al. (2024), which defines a statistical discrepancy based on the invariance properties of rank statistics. Unlike adversarial methods that rely on a learned critic to compare distributions, ISL replaces the discriminator entirely with a principled, distribution-free criterion.

At the core of ISL lies the following observation: suppose we draw K i.i.d. samples $\tilde{y}_1, \dots, \tilde{y}_K \sim \tilde{p}$ from a generative model and take a real data point $y \sim p$. If we count how many of the samples \tilde{y}_i are less than y —a quantity called the rank of y —then this rank is uniformly distributed on $\{0, \dots, K\}$ if and only if the model and data distributions coincide, i.e., $p = \tilde{p}$ (see Figure 1). This means that the rank statistic acts as an implicit test of distributional equality, without ever needing to evaluate or estimate the true data density p .

Based on this observation, we can repeat the procedure with multiple data points and define a loss function by measuring how far the empirical distribution of ranks deviates from uniformity. This yields a tractable and robust discrepancy that can be estimated efficiently using only samples and optimized via a differentiable surrogate that mimics the rank histogram. The result is a fully sample-based divergence that is invariant with respect to the true form of p , does not involve min-max games, and avoids the instability commonly found in adversarial training. Moreover, as we demonstrate in this work, ISL can be extended and adapted to tackle key limitations of current implicit methods—namely, their poor tail fidelity and tendency to collapse on modes.

While the original ISL formulation in de Frutos et al. (2024) offers a compelling alternative to adversarial training, it is essentially constrained to univariate data and assumed light-tailed target distributions. Extending ISL to multivariate by aligning marginal distributions is ineffective, as it ignores dependencies and becomes computationally intractable in high dimensional distributions. Furthermore, using simple latent priors like Gaussians restricts the model capacity to capture extreme-value behavior. Moreover, the theoretical formulation and properties of ISL have not been rigorously established.

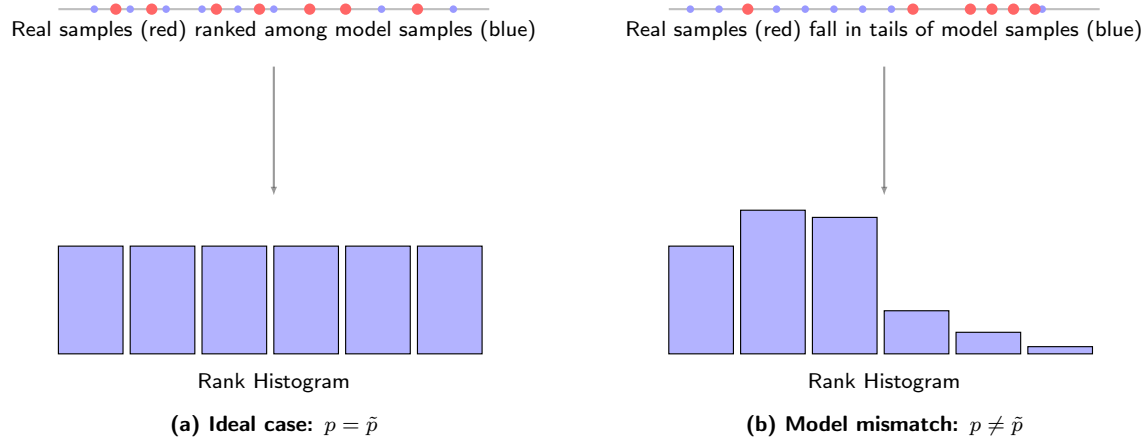


Figure 1: High-level intuition behind ISL. When the distribution \tilde{p} (distribution associated to the generator neural network) matches the data distribution p , the ranks of real samples y among generated samples $\tilde{y}_1, \dots, \tilde{y}_K$ are uniformly distributed (Figure (a)). If the distributions differ, the rank histogram becomes unbalanced (Figure (b)), revealing a difference that ISL uses to detect how well the model fits the data. Red points correspond to real data samples from p , while blue points represent samples from \tilde{p} .

1.2 Contributions

In this work, we address each of the limitations outlined above. We first formally define the ISL as a discrepancy between two probability distributions, and then prove that it constitutes a valid divergence by establishing its continuity and (almost everywhere) differentiability with respect to the generator parameters. To overcome the tail modeling issue, we introduce *Pareto-ISL*, which replaces the latent noise with a Generalized Pareto distribution and leverages unbounded generators to capture the behavior of heavy-tailed

distributions. For high-dimensional data, we propose *ISL-slicing*, a scalable extension that yields a multivariate ISL by averaging over random one-dimensional projections that preserve statistical dependencies while avoiding marginal-factorization or adversarial discriminators. Collectively, we believe that these advances make ISL a viable and competitive framework for modern generative modeling across univariate, multivariate, and heavy-tailed settings. A more detailed description of the contributions of the work is provided below.

1. Divergence guarantees. We establish that the ISL, denoted $d_K(p, \tilde{p})$, defines a valid statistical divergence. Moreover, when the generator model $g_\theta(z)$, with θ a vector of parameters and z a random input, satisfies mild regularity conditions—such as continuity and a uniform Lipschitz property— $d_K(p, \tilde{p}_\theta)$ becomes a Lipschitz-continuous function of θ , and hence differentiable almost everywhere. These properties justify the use of d_K as a theoretically sound and optimizable objective for training implicit generative models.
2. Pareto-ISL for heavy tailed data distributions. We extend ISL to model heavy-tailed distributions by replacing the standard Gaussian input with generalized Pareto noise, following principles from extreme value theory (Coles et al., 2001). This adaptation enables the generator to more accurately capture extreme-value behavior in the tails while maintaining fidelity in the central region of the distribution. Empirical results show that Pareto-ISL models distributions exhibiting heavy-tailed behavior more faithfully, improving on both Gaussian-latent ISL and adversarial schemes.
3. Scalable multivariate training with ISL-slicing. We introduce *ISL-slicing*, a scalable divergence for high-dimensional data that computes one-dimensional ISL ranks along m random projections on the $(d - 1)$ -dimensional hypersphere (where d is the dimension of the data space) and averages the results. ISL-slicing avoids the need for marginal factorization or adversarial training, maintains sensitivity to joint structure, and runs in $\mathcal{O}(mNK)$ time (where m is the number of random projections, N is the batch size, and K is the number of fictitious samples), making it efficient for high-dimensional settings.
4. Empirical validation and GAN pretraining. We demonstrate the effectiveness of ISL methods across a range of benchmarks, showing performance on par with state-of-the-art implicit models. Furthermore, we show that ISL-slicing also serves as an effective pretraining objective for GANs, significantly reducing mode collapse and enhancing sample diversity. In our experiments, ISL pretraining enables simple GANs to outperform more sophisticated (and computationally costly) adversarial models.

1.3 Organization of the paper

In Section 2 we recall basic material on rank statistics from de Frutos et al. (2024), introduce the ISL divergence and its smooth surrogate, and show that it defines a valid statistical divergence that is differentiable in the generator parameters. Section 3 presents Pareto-ISL for heavy-tailed modeling. In Section 4 we define ISL-slicing—averaging 1D ISL over random projections—to extend the proposed divergence to multivariate settings and demonstrate its effectiveness across various benchmarks. Section 5 applies these techniques to time-series forecasting. Finally, Section 6 is devoted to conclusions.

2 Rank statistics and the invariant loss function

2.1 Discrete uniform rank statistics

Let $\tilde{y}_1, \dots, \tilde{y}_K$ be a random sample from a univariate real distribution with pdf \tilde{p} and let y be a single random sample independently drawn from another distribution with pdf p . We construct the set,

$$\mathcal{A}_K := \left\{ \tilde{y} \in \{\tilde{y}_k\}_{k=1}^K : \tilde{y} \leq y \right\},$$

and the rank statistic

$$A_K := |\mathcal{A}_K|, \quad (1)$$

i.e., A_K is the number of elements in \mathcal{A}_K . The statistic A_K is a discrete r.v. that takes values in the set $\{0, \dots, K\}$; and we denote its pmf as $\mathbb{Q}_K : \{0, \dots, K\} \mapsto [0, 1]$. This pmf satisfies the following key result.

Theorem 1 *If $p = \tilde{p}$ then $\mathbb{Q}_K(n) = \frac{1}{K+1} \forall n \in \{0, \dots, K\}$, i.e., A_K is a discrete uniform r.v. on the set $\{0, \dots, K\}$.*

Proof See Elvira et al. (2021) for an explicit proof. This is a basic result that appears under different forms in the literature, e.g., in Rosenblatt (1952) or Djuric and Míguez (2010). ■

The following result generalises Theorem 2 in de Frutos et al. (2024). It establishes the continuity of the rank statistic w.r.t. the L^1 norm.

Theorem 2 *If $\|p - \tilde{p}\|_{L^1(\mathbb{R})} \leq \epsilon$ then,*

$$\frac{1}{K+1} - \epsilon \leq \mathbb{Q}_K(n) \leq \frac{1}{K+1} + \epsilon, \quad \forall n \in \{0, \dots, K\}.$$

Proof See Appendix A. ■

Remark 3 *If p and \tilde{p} have compact support $\mathcal{K} \subset \mathbb{R}$, we can generalise the previous result. By Hölder's inequality (Brézis, 2011, Theorem 4.6), we readily see that*

$$\|p - \tilde{p}\|_{L^1(\mathbb{R})} = \|\mathbb{I}_{\mathcal{K}}(p - \tilde{p})\|_{L^1(\mathbb{R})} \leq \|\mathbb{I}_{\mathcal{K}}\|_{L^q(\mathbb{R})} \|p - \tilde{p}\|_{L^{q'}(\mathbb{R})},$$

where $\frac{1}{q} + \frac{1}{q'} = 1$, $q \in [1, \infty]$, $\mathbb{I}_{\mathcal{K}}$ denotes the indicator function on \mathcal{K} , and $\|\mathbb{I}_{\mathcal{K}}\|_{L^q(\mathbb{R})} = \mathcal{L}(\mathcal{K})^{1/q}$, with $\mathcal{L}(\mathcal{K})$ being the Lebesgue measure of \mathcal{K} . Therefore, if $\|p - \tilde{p}\|_{L^{q'}(\mathbb{R})} \leq \epsilon / \mathcal{L}(\mathcal{K})^{1/q}$, then $\|p - \tilde{p}\|_{L^1(\mathbb{R})} \leq \epsilon$. This implies that Theorem 2 holds for any $L^{q'}$ with $q' \in [1, \infty]$ and not only for L^1 , provided that both p and \tilde{p} have compact support.

So far, we have shown that if the pdf of the generative model, \tilde{p} , is close to the target pdf, p , then the statistic A_K is close to uniform. A natural question to ask is whether A_K displaying a uniform distribution implies that $\tilde{p} = p$. This result is also established in de Frutos et al. (2024) and is reproduced here for convenience.

Theorem 4 Let p and \tilde{p} be pdf's of univariate real r.v.'s and let A_K be the rank statistic in Eq 1. If A_K has a discrete uniform distribution on $\{0, \dots, K\}$ for every $K \in \mathbb{N}$ then $p = \tilde{p}$ almost everywhere (a.e.).

Remark 5 If p and \tilde{p} are continuous functions then Theorem 4 implies that $p = \tilde{p}$ (everywhere).

Figure 2 illustrates how the generator density and the empirical rank-statistic pmf $\mathbb{Q}_K(n)$ evolve over the course of a training process aimed at aligning \tilde{p} with the target distribution p . As optimization proceeds, the generator density increasingly resembles the target, and the rank-statistic distribution transitions from a skewed shape to the uniform distribution expected when $\tilde{p} = p$.

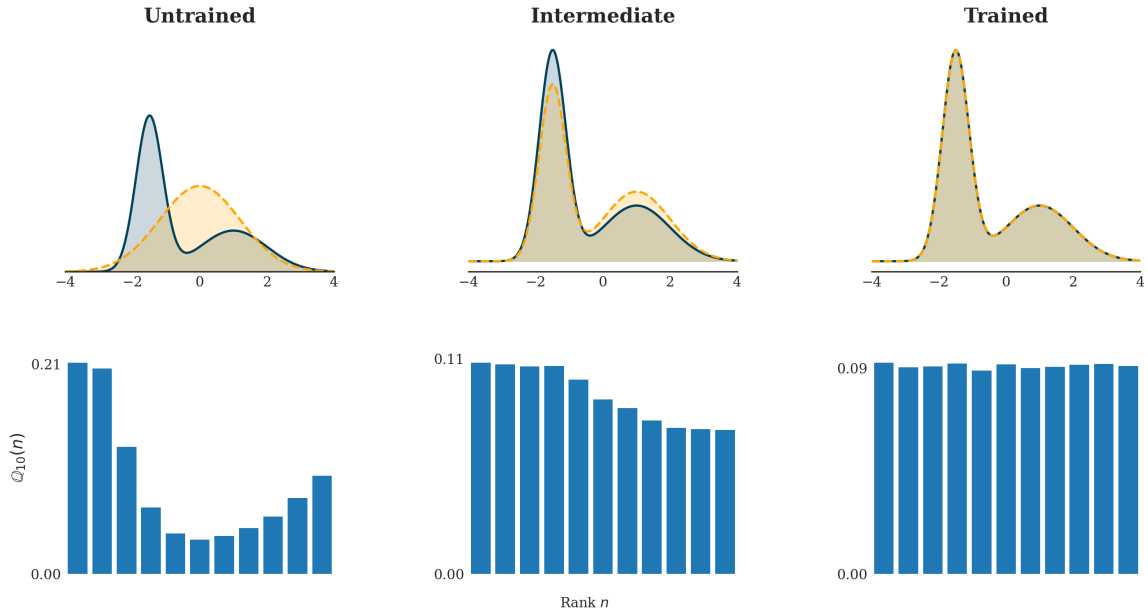


Figure 2: Evolution of generator density and rank-statistic pmf over the course of a training process aimed to align \tilde{p} with the target distribution p . Columns (left to right) show the untrained, intermediate, and trained stages. *Top row*: target density (solid blue) versus model density (dashed orange). *Bottom row*: empirical pmf $\mathbb{Q}_K(n)$ of the rank statistic. As training proceeds, the model density aligns with the target and $\mathbb{Q}_K(n)$ converges to the uniform distribution.

2.2 The invariant statistical loss function

In this subsection we build upon previous results to introduce a new discrepancy function $d_K(p, \tilde{p}) : C(\mathcal{K}) \times C(\mathcal{K}) \mapsto [0, +\infty)$ between two continuous densities on a compact set $\mathcal{K} \subset \mathbb{R}$. This function measures the ℓ_1 -norm of the difference between the pmf \mathbb{Q}_K associated with the statistic A_K and the uniform pmf, i.e.,

$$d_K(p, \tilde{p}) = \frac{1}{K+1} \left\| \frac{1}{K+1} \mathbf{1}_{K+1} - \mathbb{Q}_K \right\|_{\ell_1} = \frac{1}{K+1} \sum_{n=0}^K \left| \frac{1}{K+1} - \mathbb{Q}_K(n) \right|.$$

It is clear that $d_K(p, \tilde{p}) \geq 0$ for any pair of pdf's p and \tilde{p} . By Theorems 2 and 4, $d_K(p, \tilde{p}) = 0$ for arbitrarily large K if and only if $p = \tilde{p}$. Thus, $\lim_{K \rightarrow \infty} d_K(p, \tilde{p})$ is a probability divergence (Chen et al., 2023; Sugiyama et al., 2013). Furthermore, Theorem 2 shows that d_K is continuous w.r.t. the $L^1(\mathbb{R})$ norm, i.e., whenever $\|p - \tilde{p}\|_{L^1(\mathbb{R})} \leq \epsilon$, one has $d_K(p, \tilde{p}) \leq \epsilon$. This discrepancy measure serves as the theoretical loss function on which we build up a training procedure for implicit generative models.

The following theorem identifies two key regularity properties—continuity and differentiability—of the divergence $d_K(p, \tilde{p}_\theta)$ w.r.t. the network parameters θ of g_θ .

Theorem 6 *Let $p : \mathcal{X} \rightarrow [0, \infty)$ be a pdf, where $\mathcal{X} \subseteq \mathbb{R}$. Let Z be a real r.v. taking values in $\mathcal{Z} \subseteq \mathbb{R}$ and choose a function*

$$\begin{aligned} g : \mathcal{Z} \times \mathbb{R}^d &\rightarrow \mathcal{X}, \\ (z, \theta) &\mapsto g_\theta(z). \end{aligned}$$

Let \tilde{p}_θ denote the pdf of the r.v. $g_\theta(Z)$. Then,

1. *If g is continuous w.r.t. θ for almost every $x \in \mathcal{Z}$, then $d_K(p, \tilde{p}_\theta)$ is also continuous w.r.t. θ .*
2. *Assume that $g_\theta(z)$ satisfies the Lipschitz condition w.r.t. θ , i.e., $|g_\theta(z) - g_{\theta'}(z)| \leq L(z)\|\theta - \theta'\|$, and there is a constant $L_{\max} < +\infty$ such that $L(z) < L_{\max}$ for almost every $z \in \mathcal{Z}$. If $g_\theta(z)$ is differentiable w.r.t. z and there exists $m > 0$ such that $\inf_{(z, \theta) \in \mathcal{Z} \times \mathbb{R}^d} |g'_\theta(z)| \geq m$, then $d_K(p, \tilde{p}_\theta)$ is Lipschitz continuous w.r.t. θ , and consequently, it is differentiable a.e.*

Proof The proof of the Theorem can be found in Appendix B. ■

Theorem 6 shows that the discrepancy $d_K(p, \tilde{p}_\theta)$, which measures the difference between a fixed density p and a parametric family \tilde{p}_θ generated by $g_\theta(z)$, is continuous whenever $g_\theta(z)$ is continuous in θ . Additionally, if g_θ is Lipschitz continuous and monotonic, the discrepancy becomes differentiable a.e. However, since the dependence of the empirical distribution \mathbb{Q}_K on θ is unknown, gradient-based methods cannot be directly used to minimise $d_K(p, \tilde{p}_\theta)$ w.r.t. θ .

2.3 The surrogate invariant statistical loss function

Since the divergence $d_K(p, \tilde{p}_\theta)$ cannot be used in practice, we present a surrogate loss function that is tractable, in the sense that it can be optimised w.r.t. the network parameters θ using standard methods. The training dataset consists of a set of N i.i.d. samples, y_1, \dots, y_N , from the true data distribution, p . For each y_n , we generate K i.i.d. samples from the generative model, denoted by $\tilde{\mathbf{y}} = [\tilde{y}_1, \dots, \tilde{y}_K]^\top$, where each $\tilde{y}_i = g_\theta(z_i)$ with $z_i \sim \mathcal{N}(0, 1)$. From y_n we obtain one sample of the r.v. A_K , that we denote as $a_{K,n}$.

We replace $d_K(p, \tilde{p}_\theta)$ by a differentiable approximation and refer to this surrogate function as invariant statistical loss (ISL) (de Frutos et al., 2024). The ISL mimics the construction of a histogram from the statistics $a_{K,1}, a_{K,2}, \dots, a_{K,N}$. Given a real data point y_n , we can tally

how many of the K simulated samples in $\tilde{\mathbf{y}}$ are less than the n -th observation y_n . Specifically, one computes

$$\tilde{a}_{K,n}(y) = \sum_{i=1}^K \sigma_\alpha(y_n - \tilde{y}_i) = \sum_{i=1}^K \sigma_\alpha(y_n - g_\theta(z_i)),$$

where $z_i \sim p_z$ is a sample from a univariate distribution, and $\sigma_\alpha(x) := \sigma(\alpha x)$, with $\sigma(x) := 1/(1 + \exp(-x))$ being the sigmoid function. As we can see, $\tilde{a}_{K,n}$ is a differentiable (w.r.t. θ) approximation of the actual statistic A_K for the observation y_n . The parameter α enables us to adjust the slope of the sigmoid function to better approximate the (discrete) ‘counting’ in the construction of $\tilde{a}_{K,n}$.

A differentiable surrogate histogram is constructed from $\tilde{a}_{K,1}, \dots, \tilde{a}_{K,n}$ by leveraging a sequence of differentiable functions. These functions are designed to mimic the bins around $k \in \{0, \dots, K\}$, replacing sharp bin edges with functions that replicate bin values at k and smoothly decay outside the neighborhood of k . In our particular case, we consider radial basis function (RBF) kernels $\{\psi_k\}_{k=0}^K$ centered at $k \in \{0, \dots, K\}$ with length-scale ν^2 , i.e., $\psi_k(a) = \exp(-(a - k)^2/2\nu^2)$. Thus, the approximate normalized histogram count at bin k is given by

$$q[k] = \frac{1}{N} \sum_{i=1}^N \psi_k(\tilde{a}_{K,i}(y_i)), \quad (2)$$

for $k = 0, \dots, K$. The ISL is computed as the ℓ -norm distance between the uniform vector $\frac{1}{K+1} \mathbf{1}_{K+1}$ and the vector of empirical probabilities $\mathbf{q} = [q[0], q[1], \dots, q[K]]^\top$, namely,

$$\mathcal{L}_{ISL}(\theta, K) := \left\| \frac{1}{K+1} \mathbf{1}_{K+1} - \mathbf{q} \right\|_{\ell_1}. \quad (3)$$

Remark 7 *The ISL is a sum and composition of $C^\infty(\mathbb{R})$ functions. It is smooth w.r.t. the fictitious samples $\{\tilde{y}_i\}_{i=0}^K$ and the data y_n . As a result, its regularity aligns with that of the neural network (as a function of both its parameters and the input noise).*

The hyperparameters for the ISL method include the number of samples K , which is tunable, the activation function σ_α , and the set of basis functions $\{\psi_k\}_{k=0}^K$, specified as radial basis function (RBF) kernels with a length scale of ν^2 . These parameters control the flexibility and behavior of the model during learning.

To better illustrate the transition from discrete to differentiable rank-based histograms, Figure 3 provides a visual comparison. In Section C.1, we present a numerical study assessing how accurately the surrogate loss \mathcal{L}_{ISL} approximates the true divergence $d_K(p, \tilde{p}_\theta)$. Finally, Figure 4 outlines the full 1D ISL training pipeline, summarizing the steps involved in computing and optimizing the surrogate loss.

2.4 Progressively training by increasing K

The training procedure can be made more efficient by performing it in a sequence of increasing values of K (see de Frutos et al. (2024)). Specifically, one can select $K^{(1)} < K^{(2)} < \dots < K^{(I)}$, where I is the total number of stages and $K^{(I)} = K_{\max}$, the maximum admissible value of

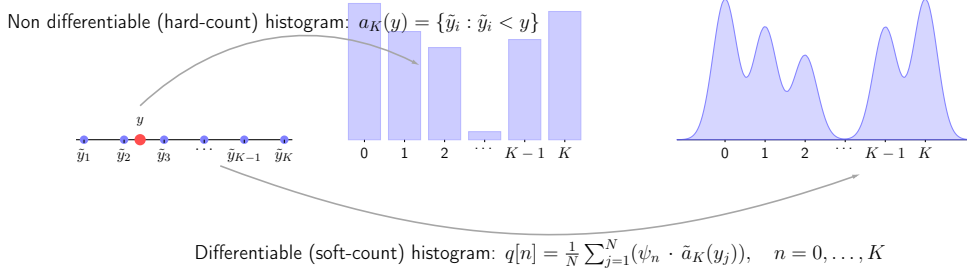


Figure 3: Hard- vs. Soft-Count Histograms via RBF-Binning. *Left*: Sorted model samples $\tilde{y}_1 \leq \dots \leq \tilde{y}_K$, with the observed value y highlighted in red. *Middle*: Standard hard-count histogram: each bin i tallies the number of model samples below y , i.e. $a_K(y) = |\{\tilde{y}_j : \tilde{y}_j < y\}|$, yielding discrete, integer counts per bin. *Right*: Differentiable soft-count histogram obtained by RBF-binning, where each \tilde{y}_j contributes fractionally to every bin according to $q[n] = \frac{1}{N} \sum_{j=1}^N \psi_n(\tilde{y}_j, y)$ for each $n \in \{0, \dots, K\}$, giving a smooth, continuous pmf.

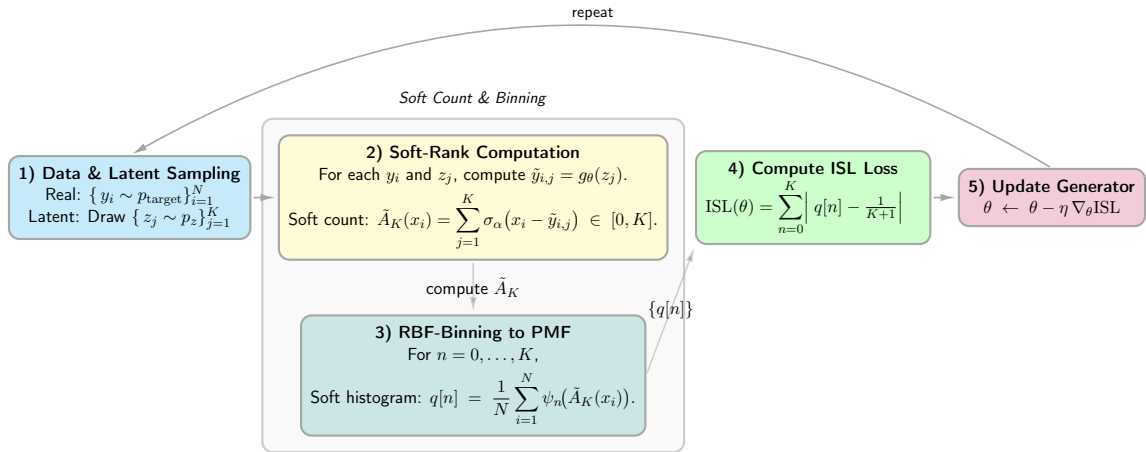


Figure 4: 1D ISL Training Pipeline. First, real data samples $y_i \sim p_{\text{target}}$ and latent inputs $z_j \sim p_z$ are drawn (Step 1). Next, for each pair (y_i, z_j) , the network output $\tilde{y}_{i,j} = g_\theta(z_j)$ is compared to y_i via a smooth indicator function to produce *soft counts* $\tilde{A}_K(x_i) \in [0, K]$ (Step 2). These counts are then converted into a *continuous pseudo-PMF* $q[n]$ over ranks $n = 0, \dots, K$ using RBF kernels (Step 3). The ISL loss is computed as the L^1 -distance between $q[n]$ and the uniform distribution (Step 4). Finally, θ is updated by gradient descent on this loss (Step 5), and the process repeats. This pipeline yields a fully differentiable surrogate for the invariant statistical loss suitable for end-to-end training.

K . The iterative training scheme is outlined in Algorithm 1. The gain in efficiency of the progressive training procedure compared to a scheme with fixed K is illustrated in Appendix C.2.

3 Pareto-ISL

As shown in de Frutos et al. (2024), ISL outperforms other generative methods in learning the central regions of typical 1D distributions. However, Figure 5 indicates that when standard Gaussian noise is used as an input, NNs struggle to capture the tails of Cauchy

Algorithm 1 Progressively training by increasing K

```

1: Input Neural network  $g_\theta$ ; hyperparameters  $N$ ; number of epochs; training data  $\{y_i\}_{i=1}^N$ ;
    $K_{\max}$  maximum admissible value of  $K$ .
2: Output Trained neural network  $g_\theta$ .
3:  $K = K^{(1)}$ 
4: For  $t = 1, \dots, \text{epochs}$  do
5:   Train  $g_\theta$  using ISL loss function:  $\mathcal{L}_{\text{ISL}}(\theta, K^{(i)})$ 
6:   Compute  $\{a_{K^{(i)},1}, \dots, a_{K^{(i)},N}\}$ 
7:   Compute Pearson  $\chi^2$  test against  $\mathbb{Q}_{K^{(i)}}$  using  $\{a_{K^{(i)},1}, \dots, a_{K^{(i)},N}\}$ 
8:   If hypothesis " $A_K$  is uniform" is accepted and  $K^{(i)} < K_{\max}$  do
9:     Set  $K = K^{(i+1)}$ 
10:  return  $g_\theta$ 

```

mixtures, since compactly supported inputs cannot produce unbounded pdfs (which we will refer to as unbounded distributions). This issue can be addressed by using input noise from a generalized Pareto distribution (GPD). In this section, we introduce Pareto-ISL, which utilizes a GPD for input noise, and demonstrate its effectiveness in learning heavy-tailed distributions.

3.1 Tail distributions and extreme value theory

The conditional excess distribution function $F_u(y)$ provides a key tool for analyzing the tail of a distribution by focusing on exceedances over a specified threshold u . By conditioning on large values, it isolates the behavior of the distribution in its tail, where extreme or rare events are more likely to occur. In the context of extreme value theory, for sufficiently high thresholds u , the conditional excess distribution function converges to the GPD. The GPD, parameterized by the tail index ξ and scaling parameter σ , provides a flexible model for the tail, allowing us to characterize its heaviness and the probability of extreme values.

The following definitions are taken from Huster et al. (2021) and provided here for convenience.

Definition 8 *The conditional excess distribution function with threshold $u \in \mathbb{R}$ is defined as*

$$F_u(y) = \mathbb{P}(X - u \leq y | X > u) = \frac{F(u + y) - F(u)}{1 - F(u)}.$$

Definition 9 *The GPD, parametrized by tail index $\xi \in \mathbb{R}$ and scaling parameter $\sigma \in \mathbb{R}^+$, has the following complementary cumulative distribution function (CCDF)*

$$S(z; \xi, \sigma) = \begin{cases} (1 + \xi z / \sigma)^{-1/\xi}, & \text{for } \xi \neq 0, \\ e^{-z/\sigma}, & \text{for } \xi = 0. \end{cases}$$

Lipschitz continuous functions map bounded distributions to bounded ones (Evans, 2018, Chapter 3), limiting the ability of NNs to model heavy-tailed distributions. To address this, unbounded input distributions are required.

To construct unbounded NN generators, recall that piecewise linear (PWL) functions, (which include operations like rectified linear unit (ReLU), leaky ReLU, linear layers, addition, and batch normalization), are closed under composition (Arora et al., 2016, Theorem 2.1) and are unbounded, making them ideal for constructing generators that approximate heavy-tailed distributions.

We then define a Pareto-ISL generator, g^{PWL} , as a piecewise linear generator driven by an input from a GPD with tail index ξ , and trained using ISL. Estimators such as Hill's (Resnick and Stărică, 1997) can be used to estimate ξ , aiding in the accurate modeling of heavy-tailed behavior.

Definition 10 (Pareto-ISL) *Let $z_\xi = (U^{-\xi} - 1)/\xi$, where $U \sim \mathcal{U}(0, 1)$, be a GPD r.v. with tail index ξ and CCDF $S(x; \xi, 1)$. A Pareto-ISL generator is g_θ^{PWL} , with an input distribution z_ξ parameterized by ξ , and output distribution $y_\xi = g_\theta^{PWL}(z_\xi)$.*

The Pickands-Balkema-de Haan theorem (Balkema and De Haan, 1974) states that for a wide range of probability distributions, the conditional excess distribution function converges to the GPD as the threshold u increases. This applies to distributions like Gaussian, Laplacian, Cauchy, Lévy, Student-t, and Pareto. Building on this result and (Huster et al., 2021, Theorem 2), a generator constructed using g^{PWL} with a GPD input can effectively approximate the conditional excess distribution of heavy-tailed distributions. Specifically, if y_ξ has unbounded support, the conditional excess distribution $F_u(y)$ of y_ξ converges to $S(y; \xi, \sigma)$ for some $\sigma \in \mathbb{R}^+$. This indicates that ISL-Pareto is especially well-suited for these types of problems, outperforming other implicit methods, including ISL with non-Pareto noise, as we demonstrate in the following subsection.

3.2 Comparison of Pareto-ISL and standard ISL in learning a Cauchy mixture

In Figure 5, we compare Pareto-ISL against standard ISL where the data distribution is a two-component Cauchy mixture with locations at -1.0 and 1.0 , and scales 0.7 and 0.85 . All generators use a four-layer multilayer perceptron (MLP) with 35 units per layer and ReLU activation. Generators are trained with ISL using $K = 20$, $N = 1000$, and a learning rate of 10^{-3} . For Pareto-ISL, the tail parameter is set to $\xi = 1$, aligning GPD noise with the tail index of the Cauchy mixture. Introducing GPD noise improves tail approximation and enhances the modeling of the central part of the target distribution, as demonstrated in the logarithmic-scale (bottom row) and linear-scale (top row) of Figure 5.

In C.3, we present a multidimensional heavy-tailed distribution and compare Pareto-ISL to ISL with Gaussian noise (results shown in Figure 14).

3.3 Performance evaluation of Pareto-ISL compared to other implicit generative models

In a second experiment, we evaluate the performance of Pareto-ISL as compared to different GANs. For this comparison, we consider four data distributions, including a Cauchy distribution with location parameter 1 and scale parameter 2 (labeled Cauchy(1, 2)), a Pareto distribution with scale parameter 1 and shape parameter 1 (labeled Pareto(1, 1)) and two mixture distributions, labeled Model₃ and Model₄. Model₃ is a mixture of a $\mathcal{N}(-5, 2)$

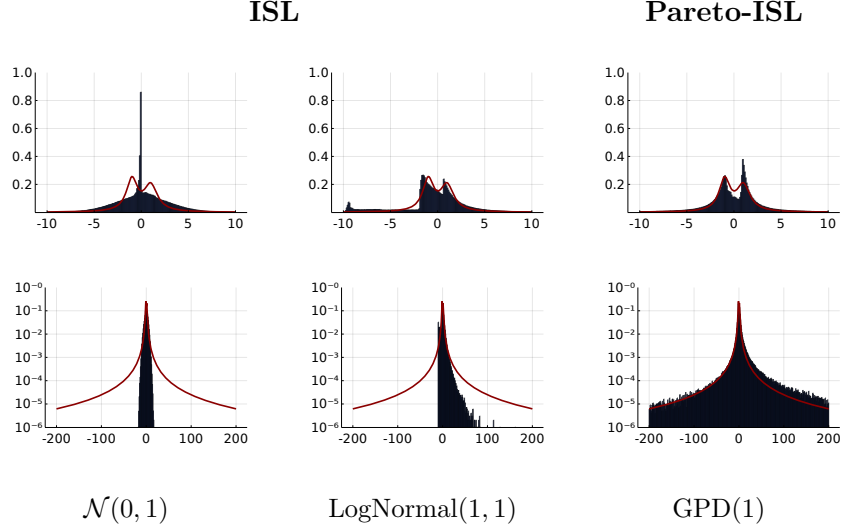


Figure 5: Pdfs approximated by generators with various tail behaviors. The noise input for each subplot is given by the subcaption of the corresponding column. Generators are trained on a mixture of Cauchy distributions, with the true density displayed in red. The top row presents the central region of the distributions on a linear scale, while the bottom row highlights the tails on a logarithmic scale.

distribution and a Pareto(5, 1) distribution, while Model₄ is a mixture of a Cauchy(−1, 0.7) distribution and a Cauchy(1, 0.85) distribution.

As generator NN, we use a 4-layer MLP with 7, 13, 7 and 1 units at the corresponding layers. As activation function we use a ReLU. We train each setting up to 10^4 epochs with 10^{-2} learning rate using Adam. We compare Pareto-ISL, GAN, Wasserstein GAN (WGAN) from (Arjovsky et al., 2017), and maximum mean discrepancy GAN (MMD-GAN) proposed in Li et al. (2017) using KSD (Kolmogorov-Smirnov distance), MAE (mean absolute error), and MSE (mean squared error) error metrics, defined as follows

$$\text{KSD} = \sup_{x \in \mathbb{R}} |F(x) - \tilde{F}(x)|, \quad \text{MAE} = \int_{\mathbb{R}} |g(z) - g_{\theta}(z)| p_z(z) dz, \quad \text{MSE} = \int_{\mathbb{R}} (g(z) - g_{\theta}(z))^2 p_z(z) dz.$$

where F and \tilde{F} represent, respectively, the cdfs of the data distribution and the r.v. generated by the neural network g_{θ} with input $z \sim p_z$. Moreover, g denotes the optimal transformation of the data distribution. The results are detailed in Table 1.

Target	Pareto-ISL			GAN			WGAN			MMD-GAN		
	KSD	MAE	MSE	KSD	MAE	MSE	KSD	MAE	MSE	KSD	MAE	MSE
Cauchy(1,2)	1.90e-3	1.42	15.78	0.08	8.96	8207.00	0.03	10.57	8127.00	0.03	9.68	57975.00
Pareto(1,1)	5.30e-3	1.16	2.41	0.10	12.64	114970.00	0.49	7.64	7062.00	0.50	9.02	10674.00
Model ₃	0.02	0.47	0.33	0.19	0.45		1.61	0.30	3.04	13.13	0.56	3.20
Model ₄	0.01	0.61	1.05	0.02	0.77		2.75	0.03	2.63	66.06	0.02	0.66
												2.60

Table 1: Comparison of Pareto-ISL results with vanilla GAN, WGAN, and MMD-GAN when input noise is a standard Gaussian, $K_{\max} = 10$, epochs=1000, and $N = 1000$. The best result for each metric is highlighted in bold.

3.4 Assessment of Pareto-ISL on heavy-tailed datasets

In this third experiment, we demonstrate the effectiveness of the Pareto-ISL scheme on two univariate heavy-tailed datasets:

- 136 million keystrokes (**Keystrokes**): this dataset includes inter-arrival times between keystrokes for a variety of users.
- Wikipedia web traffic (**Wiki Traffic**): this dataset includes the daily number of views of Wikipedia articles during 2015 and 2016.

Our assessment uses two metrics. First, we compute the KSD to compare the data distribution and the generated distribution. Then, we calculate the area A_{CCDF} between the log-log plots of the CCDFs of data and generated samples, indicating how well the tails of the distributions match. For n real samples, we have

$$A_{CCDF} = \sum_{i=1}^n \left[\log \left(F_p^{-1} \left(\frac{i}{n} \right) \right) - \log \left(\tilde{F}_{\tilde{p}}^{-1} \left(\frac{i}{n} \right) \right) \right] \log \left(\frac{i+1}{i} \right),$$

where F_p^{-1} and $\tilde{F}_{\tilde{p}}^{-1}$ are the inverse empirical CCDFs for the data distribution p and the generated distribution \tilde{p} , respectively.

We use a common network architecture and training procedure for all experiments. The network consists of 4 fully connected layers with 32 hidden units per layer and ReLU activations. Results are shown in Table 2.

Method	Keystrokes		Wiki Traffic	
	KS	A_{CCDF}	KS	A_{CCDF}
Uniform (ISL)	0.087	6.20	0.025	10.30
Normal (ISL)	0.090	2.70	0.023	8.60
Lognormal (ISL)	0.096	1.70	0.019	9.50
Pareto GAN (Huster et al., 2021)	0.013	21.10	0.017	4.50
Gamma–Weibull KDE (Markovich, 2016)	0.050	1.70	0.075	1.50
Pareto-ISL	0.006	1.4	0.017	1.19

Table 2: Pareto-ISL outperforms ISL variants (Uniform, Normal, Lognormal), Pareto GAN (Huster et al., 2021), and Gamma–Weibull KDE (Markovich, 2016) in tail estimation (A_{CCDF}), while also achieving lower KS distance.

4 ISL-slicing: A random projections-based approach

Machine learning datasets are often multi-dimensional. Building on Bonneel et al. (2015) and Kolouri et al. (2019), we extend the one-dimensional loss function \mathcal{L}_{ISL} to a general metric for higher dimensions. We do this by randomly projecting high-dimensional data onto various 1D subspaces, specifically in all possible directions $s \in \mathbb{S}^d$, where \mathbb{S}^d is the unit hypersphere in $d + 1$ -dimensional space.

Let x be a $(d+1)$ -dimensional r.v. and let $s \in \mathbb{R}^{d+1}$ be a deterministic vector. We denote by $s\#p$ the pdf of the real r.v. $y = s^\top x$. Using this notation we define the *sliced ISL distance* between distributions with pdfs p and \tilde{p} as

$$d_K^{\mathbb{S}^d}(p, \tilde{p}) := \int_{s \in \mathbb{S}^d} d_K^s(p, \tilde{p}) ds,$$

where $d_K^s(p, \tilde{p}) = d_K(s\#p, s\#\tilde{p})$.

Since the expectation in the definition of the sliced ISL distance is computationally intractable, we approximate it using Monte Carlo sampling. Specifically, we choose a pdf q on \mathbb{S}^d and sample directions $s_i \sim q$, for $i = 1, \dots, m$. Then, the Monte Carlo approximation of the sliced ISL distance is

$$\tilde{d}_K^{\mathbb{S}^d}(p, \tilde{p}) = \frac{1}{m} \sum_{i=1}^m d_K(s_i\#p, s_i\#\tilde{p}). \quad (4)$$

If $\tilde{p} \equiv \tilde{p}_\theta$ is the pdf of the r.v. $y = g_\theta(z)$, $z \sim p_z$, i.e., the output of a NN with random input z and parameters θ , then one can use $\tilde{d}_K^{\mathbb{S}^d}(p, \tilde{p}_\theta)$ as a loss function to train the NN.

Remark 11 *In practice, we use the surrogate loss (see Section 2.3) to approximate $d_K(s_i\#p, s_i\#\tilde{p}_\theta)$ in Eq.4, and sample random vectors from the unit sphere. Randomly chosen vectors from the unit sphere in a high-dimensional space are typically almost orthogonal. More precisely, (see Gorban and Tyukin (2018))*

$$\mathbb{P}\left(\left|\frac{v_1^\top v_0}{\|v_1\|_2 \|v_0\|_2}\right| < \epsilon\right) > 1 - 2e^{-\frac{1}{2}d\epsilon^2},$$

where v_0 and v_1 are uniformly distributed random vectors, and ϵ is a small positive constant.

The pseudocode for training implicit models using the proposed random projection method, referred to as the *ISL-slicing algorithm*, is provided in Algorithm 2.

4.1 Random projections vs. marginals on high-dimensional data

Following Saatci and Wilson (2017), we conduct experiments on a multi-modal synthetic dataset. Specifically, we generate D -dimensional synthetic data from the model

$$\begin{cases} \mathbf{z} \sim \mathcal{N}(0, 10 \cdot I_d), & \mathbf{A} \sim \mathcal{N}(0, I_{D \times d}), & \epsilon \sim \mathcal{N}(0, 0.01 \cdot I_D), \\ \mathbf{x} = \mathbf{A}\mathbf{z} + \epsilon, & d \ll D. \end{cases}$$

In these experiments, we fit a standard GAN to a dataset where $D = 100$ and $d = 2$. The generator is a 3-layer fully connected neural network with 10, 1000, and 100 units, respectively, using ReLU activations throughout.

Figure 6 illustrates the performance of random projections (ISL-slicing) when compared with that of the marginal pdf-based method from de Frutos et al. (2024). Our results show that even with a limited number of projections, ISL-slicing achieves a lower Jensen-Shannon divergence (JS-Divergence) w.r.t. the true distribution, as estimated by kernel density. This approach also significantly reduces computation time per iteration compared to ISL marginals, since the number of projections is a fraction of the total marginals. Specifically, it took 10x and 5x less execution time, respectively, to obtain the results shown in Figures 6a and 6b using the slicing method compared to the marginals method.

Algorithm 2 ISL-slicing algorithm

```

1: Input Neural network  $g_\theta$ ; hyperparameter  $K$ ; number of epochs  $N$ ; batch size  $M$ ;
   training data  $\{y_i\}_{i=1}^N$ ; number of randomly chosen projections  $m$ .
2: Output Trained neural network  $g_\theta$ .
3: For  $t = 1, \dots$ , epochs do
4:   For iteration  $= 1, \dots, N/M$  do
5:      $L = 0$ 
6:     Sample uniformly distributed random projection directions  $\hat{\mathbb{S}}^d = \{s_{1:m}\}$ 
7:     Select  $M$  samples from  $\{y_j\}_{j=1}^N$  at random
8:     For each  $s \in \hat{\mathbb{S}}^d$  do
9:        $\{z_i\}_{i=1}^K \sim \mathcal{N}(\mathbf{0}, I)$ 
10:       $\mathbf{q} = \frac{1}{M} \sum_{j=1}^M \psi_k \left( \sum_{i=1}^K \sigma_\alpha(s^\top y_j - s^\top g_\theta(z_i)) \right)$ 
11:       $L \leftarrow L + \nabla_\theta \left\| \frac{1}{K+1} \mathbf{1}_{K+1} - \mathbf{q} \right\|_2$ 
12:      Backpropagation( $g_\theta, \nabla_\theta L / m$ )
13:   return  $g_\theta$ 

```

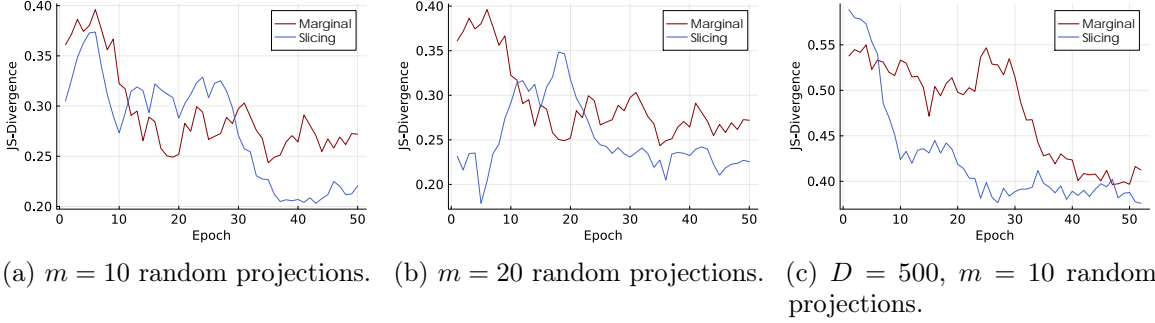


Figure 6: Performance evaluation of ISL-slicing vs ISL marginal methods on a synthetic dataset. Plots (a) and (b) correspond to $D = 100$ with different random projections ($m = 10$ and $m = 20$). Plot (c) corresponds to $D = 500$ and $m = 10$. The hyperparameters are $K = 10$, $N = 1000$ and learning rate of 10^{-4} .

4.2 Experiments on 2D distributions

We begin by examining simple 2D distributions characterized by different topological structures: one distribution with two modes, another with eight modes, and a third featuring two rings. Our objective is to assess the ability of the ISL-slicing method to fully capture the support of these distributions. We compare our approach to normalizing flows and GANs, using KL-divergence and visual assessment as metrics.

For GAN, WGAN, and ISL, we use a 4-layer MLP generator with a 2D input sampled from a standard normal distribution. Each layer has 32 units and uses the hyperbolic tangent activation. The discriminator is an MLP with 128 units per layer, using ReLU activations except for the final sigmoid layer. We used a batch size of 1000 and optimized the

critic-to-generator update ratio over $\{1:1, 2:1, 3:1, 4:1, 5:1\}$ for GAN and WGAN. The learning rate was chosen from $\{10^{-2}, 10^{-3}, 10^{-4}, 10^{-5}\}$. For ISL, we set $K = 10$, $N = 1000$, $m = 10$ random projections, and a learning rate of 10^{-3} . For the normalizing flow model, we used the RealNVP architecture from Dinh et al. (2016), with 4 layers of affine coupling blocks, parameterized by MLPs with two hidden layers of 32 units each. The learning rate was set to $5 \cdot 10^{-5}$, using the implementation from Stimper et al. (2023). All methods were trained for 1000 epochs, with optimization performed using the ADAM algorithm.

Figure 7 highlights the challenges of training GANs, particularly their susceptibility to mode collapse. In contrast, normalizing flow methods preserve topology via invertibility constraints but struggle to model complex structures, often forming a single connected component due to density filaments. Our method overcomes this by capturing the full distribution support and distinguishing between connected components, as seen in the **Dual Moon** example. However, ISL can fill regions between modes, as seen in the **Circle of Gaussians**, an issue mitigated by increasing K . Alternatively, combining a pretrained network with ISL (trained for 100 epochs) and a GAN yielded the best results (method denoted as ISL+GAN), capturing full support while excluding zero-density regions. This approach is detailed further in Section 4.3. We also estimate the KL-divergences between the target and model distributions, as listed in Table 3. In all cases, the ISL method, and particularly the ISL+GAN approach, outperform the respective baselines.

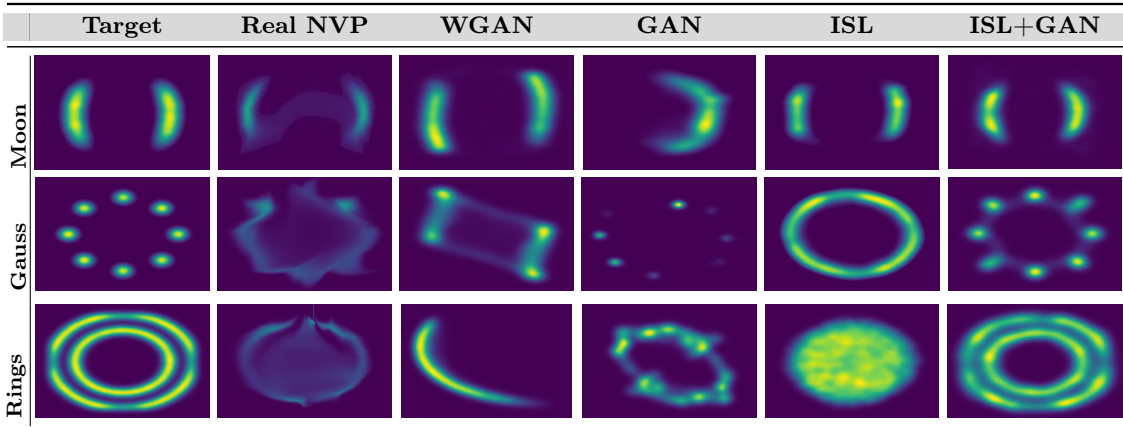


Figure 7: Comparison of the performance of various generative methods—Real NVP, WGAN, GAN, ISL-slicing, and GAN pretrained with ISL to approximate three complex 2D distributions: the **Moon**, **Gauss**, and **Rings** datasets—referred to as Dual Moon, Circle Gaussian, and Two Rings, respectively. For a detailed description of the dataset, refer to Stimper et al. (2023). The first column shows the target distributions, while the subsequent columns display the results generated by Real NVP, WGAN, GAN, ISL-slicing, and GAN pretrained with ISL, in that order.

4.3 ISL-pretrained GANs for robust mode coverage in 2D grids

In this experiment, we explore how ISL-pretrained GANs improve mode coverage on the **2D-Ring** and **2D-Grid** datasets, benchmarks commonly used in generative model evaluation. The **2D-Ring** dataset consists of eight Gaussian distributions arranged in a circle, while the **2D-Grid** dataset has twenty-five Gaussians on a grid. We first pretrain with ISL-slicing to

Method / Dataset	Real NVP	GAN	WGAN	ISL	ISL+GAN
Dual moon	1.77	1.23	1.02	0.43	0.30
Circle of Gaussians	2.59	2.24	2.38	1.61	0.46
Two rings	2.69	1.46	2.74	0.56	0.38

Table 3: Performance comparison of generative methods on 2D distributions. The table summarizes KL-divergence results for Real NVP, GAN, WGAN, and ISL on **Dual Moon**, **Circle of Gaussians**, and **Two Rings**. Lower values indicate better performance.

ensure comprehensive mode coverage, then fine-tune with a GAN. Performance was compared to other GANs using two metrics: the number of covered modes (`#modes`) and the percentage of high-quality samples (`%HQ`). A mode is covered if generated samples fall within three standard deviations of the Gaussian center, which also defines high-quality samples. The second metric represents their proportion among all generated samples.

We follow the experimental settings for GAN and WGAN as outlined by Luo and Yang (2024). The generator is a 4-layer MLP with 128 units per layer and ReLU activation, while the discriminator is an MLP with 128 units, using ReLU except for a sigmoid in the final layer. We use a batch size of 128, a 1:1 critic-to-generator update ratio, and learning rates of 10^{-4} for GAN and 10^{-5} for WGAN, both optimized using ADAM. ISL was run for 250 epochs with $K = 10$, $N = 1000$, and $m = 5$ random projections, capturing the full support of the distribution. The GAN is then trained for 30000 epochs. The results presented in Table 4 and Figure 8 compare our method with other techniques for addressing mode collapse in GANs. They demonstrate that our approach performs on par with more advanced methods, such as DynGAN (a semi-supervised technique, see Luo and Yang (2024)) and BourGAN (computationally intensive, see Xiao et al. (2018)), while offering greater simplicity.

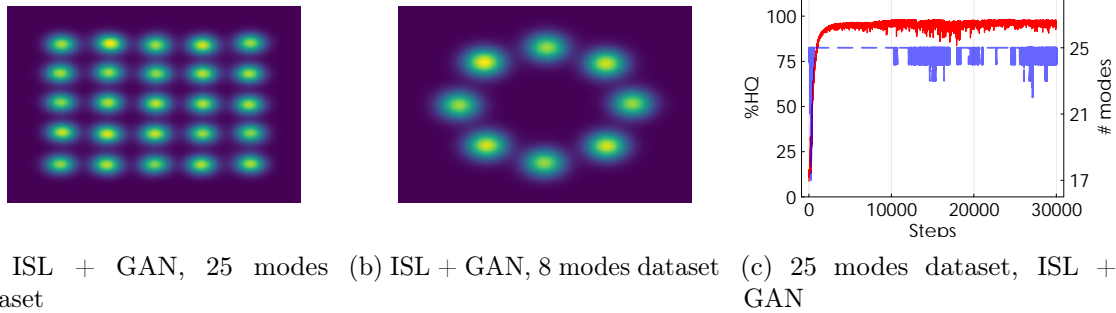
Finally, we conduct a robustness experiment comparing the performance of a WGAN with suboptimal hyperparameters to the same WGAN after ISL pretraining. Both use the same generator and discriminator architectures described in Section 4.2. The WGAN hyperparameters include a batch size of 1000, a critic-to-generator update ratio optimized over $\{1:1, 2:1, 3:1, 4:1, 5:1\}$, and a learning rate of 10^{-5} . For ISL, we use $K = 10$, $N = 1000$, $m = 10$ random projections, and a learning rate of 10^{-3} . Numerical results are displayed in Table 5. Additional experiments with batch sizes $\{64, 128, 252, 512\}$ and optimized critic-to-generator ratios are shown in Table 6. ISL-pretrained WGAN consistently outperforms standard WGAN across all ratios and batch sizes, detecting all 8 modes and producing high-quality samples. This shows that ISL pretraining significantly enhances stability and performance, leading to more robust GAN training. Once all modes are captured by ISL, a low learning rate allows the generator to improve high-quality metrics while maintaining full distribution coverage.

4.4 Addressing mode collapse on MNIST and FMNIST

In this section, we assess the effectiveness of the ISL-slicing for generating high-dimensional images. We integrate the ISL-slicing loss into the deep convolutional GAN (DCGAN) generator’s training (Radford et al., 2015) and evaluate its performance on the MNIST and Fashion-MNIST benchmarks. Following Sajjadi et al. (2018), we characterize the quality

Method	2D-Ring		2D-Grid	
	#modes	%HQ	#modes	%HQ
GAN (Goodfellow et al., 2014)	6.3	98.2	17.1	92.5
VEEGAN (Srivastava et al., 2017)	8.0	86.8	24.4	74.2
Pointwise (Zhong et al., 2019)	8.0	87.5	25.0	76.7
BourGAN (Xiao et al., 2018)	8.0	99.9	25.0	94.9
WGAN (Arjovsky et al., 2017)	7.7	86.4	24.8	83.7
DynGAN (Luo and Yang, 2024)	8.0	99.5	25.0	96.0
ISL + GAN	8.0	97.9	24.6	96.8
ISL + WGAN	8.0	97.4	25.0	96.0

Table 4: Quantitative results on synthetic 2D-mode benchmarks. #modes is the number of modes covered; %HQ is the percentage of high-quality samples (higher is better).



(a) ISL + GAN, 25 modes dataset (b) ISL + GAN, 8 modes dataset (c) 25 modes dataset, ISL + GAN

Figure 8: ISL + GAN on 25 and 8 modes datasets (plots (a) and (b), respectively) with $K = 10$, $N = 1000$, ISL learning rate of 10^{-3} for 250 epochs, and GAN with a batch size of 128, 1:1 critic-generator ratio, and learning rate of 10^{-4} for 30000 epochs. Plot (c) shows the coverage of the 2D-Grid dataset, highlighting the number of modes covered (#modes, blue) and high-quality samples (%HQ, red) during GAN training after ISL pretraining.

and diversity of generated images by reporting precision (as a proxy for fidelity) and recall (as a proxy for diversity). We train each model for 40 epochs with a batch size of 128. For the pretrained variants, we first ran 20 epochs under the sliced dual-ISL objective (using 20 random projections) and then continued with 40 epochs of standard DCGAN training.

In Table 7, we compare our results to those of other implicit generative models. On MNIST, our straightforward ISL-based model matches the recall of five-discriminator GANs (Durugkar et al., 2016; Choi and Han, 2022) while using only one-third the number of parameters. Moreover, pretraining the generator with sliced-ISL and then fine-tuning under the standard adversarial loss delivers state-of-the-art precision and recall.

On Fashion-MNIST, our model almost ties the recall of MCL-GAN’s and, although the recall of GMAN is higher, we outperform it in precision. This shows that despite relying on a simpler architecture, ISL can achieve competitive recall and precision across diverse image-generation benchmarks.

Critics	WGAN			ISL+WGAN		
	#modes	%HQ	KL div	#modes	%HQ	KL div
1:1	3.70	40.99	33.99	8.0	97.74	0.51
1:2	7.00	0.07	59.58	8.0	98.43	0.47
1:3	8.00	0.63	57.05	8.0	97.39	0.55
1:4	8.00	0.44	59.18	8.0	98.07	0.78
1:5	8.00	0.19	56.83	8.0	98.24	0.72

Table 5: Comparison of WGAN and ISL + WGAN on the 2D-Ring dataset.

Batch Size	WGAN			ISL+WGAN		
	#modes	%HQ	KL div	#modes	%HQ	KL div
64	6.10	30.01	40.52	8.0	99.31	0.82
128	4.50	19.94	47.29	8.0	98.22	1.20
252	3.10	19.98	46.57	8.0	89.70	2.24
512	3.50	29.97	41.19	8.0	95.18	1.71

Table 6: Comparison of WGAN and ISL + WGAN with different batch sizes.

Dataset	Method	F-score		P&R	
		$F_{1/8} \uparrow$	$F_8 \uparrow$	Precision \uparrow	Recall \uparrow
MNIST	ISL (m=20)	85.00 ± 0.32	95.17 ± 1.76	84.85 ± 1.20	95.35 ± 1.39
	ISL (m=50)	85.69 ± 0.29	95.81 ± 1.24	85.55 ± 1.11	96.23 ± 1.98
	DCGAN	93.58 ± 0.64	75.66 ± 1.46	93.85 ± 1.45	75.43 ± 2.56
	ISL + DCGAN	93.58 ± 0.84	95.82 ± 1.61	94.03 ± 1.82	96.68 ± 2.42
	GMAN	97.60 ± 0.70	96.81 ± 1.71	97.60 ± 1.82	96.80 ± 2.42
	MCL-GAN	97.71 ± 0.19	98.49 ± 1.57	97.70 ± 1.33	98.50 ± 2.15
FMNIST	ISL (m=20)	81.84 ± 0.11	91.08 ± 1.83	81.48 ± 1.43	91.49 ± 2.15
	ISL (m=50)	83.90 ± 0.09	91.18 ± 1.57	84.08 ± 1.31	92.92 ± 1.23
	DCGAN	86.14 ± 0.11	88.92 ± 1.51	86.60 ± 1.58	88.97 ± 1.33
	ISL + DCGAN	91.43 ± 0.19	91.87 ± 1.57	91.88 ± 1.35	92.42 ± 1.47
	GMAN	90.97 ± 0.09	95.43 ± 1.12	90.90 ± 1.33	95.50 ± 2.25
	MCL-GAN	97.62 ± 0.09	92.97 ± 1.28	97.70 ± 1.33	92.90 ± 2.31

Table 7: Quantitative results on MNIST and Fashion-MNIST (28×28), reporting $F_{1/8}$ and F_8 (β -weighted harmonic means of precision and recall), precision, and recall (mean \pm std, %). We compare ISL (m=20, 50), standard DCGAN (with and without ISL pretraining), GMAN, and MCL-GAN. Bold entries mark the best score per column; higher is better.

Figure 9 compares the class-frequency distributions produced by the sliced ISL model (trained for 40 epochs with $m = 50$ random projections) against those generated by a conventional DCGAN. Our model generates all ten digit classes with nearly uniform frequency whereas the DCGAN displays marked class imbalances. To estimate these frequencies, we sampled 10,000 images from each model and labeled them using a pretrained digit classifier. Under a one-sample Kolmogorov–Smirnov test for uniformity on 10,000 samples, the sliced-ISL model yielded a p-value $p = 0.062$, whereas the DCGAN produced $p = 0.742$ —reflecting a much closer match to the ideal uniform distribution.

Figure 10 shows the precision and recall of the ISL model on MNIST in an ablation study with $m = 20$ and $m = 100$ random projections. With just $m = 20$ projections, the model delivers robust performance; increasing to $m = 100$ yields only marginal improvements in these metrics. Monte Carlo sampling error for the sliced-ISL estimator scales as $1/\sqrt{m}$, so initial increases in m deliver significant gains but further increases produce only marginal improvements, explaining the observed performance plateau.

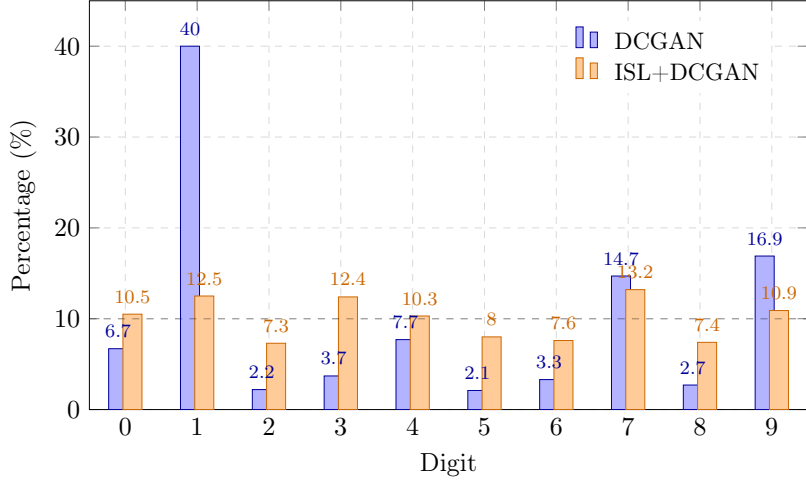


Figure 9: Digit-frequency comparison for DCGAN vs. ISL+DCGAN. The dashed line marks the ideal 10% for each class.

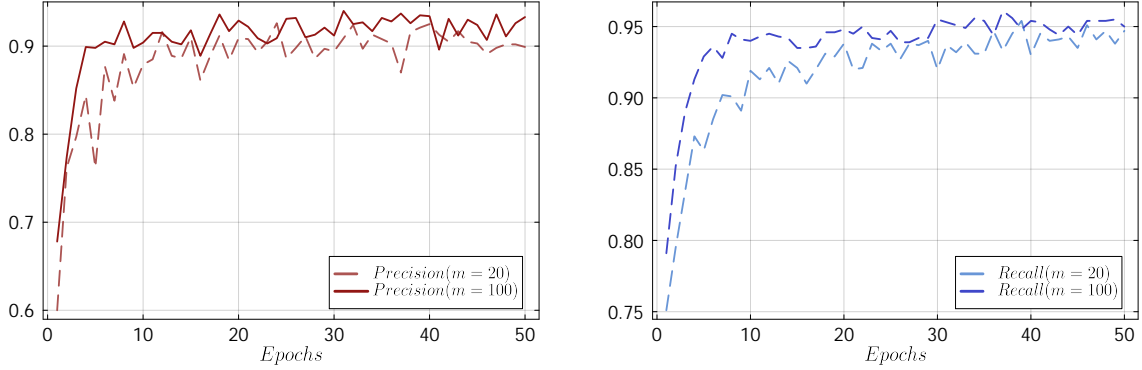
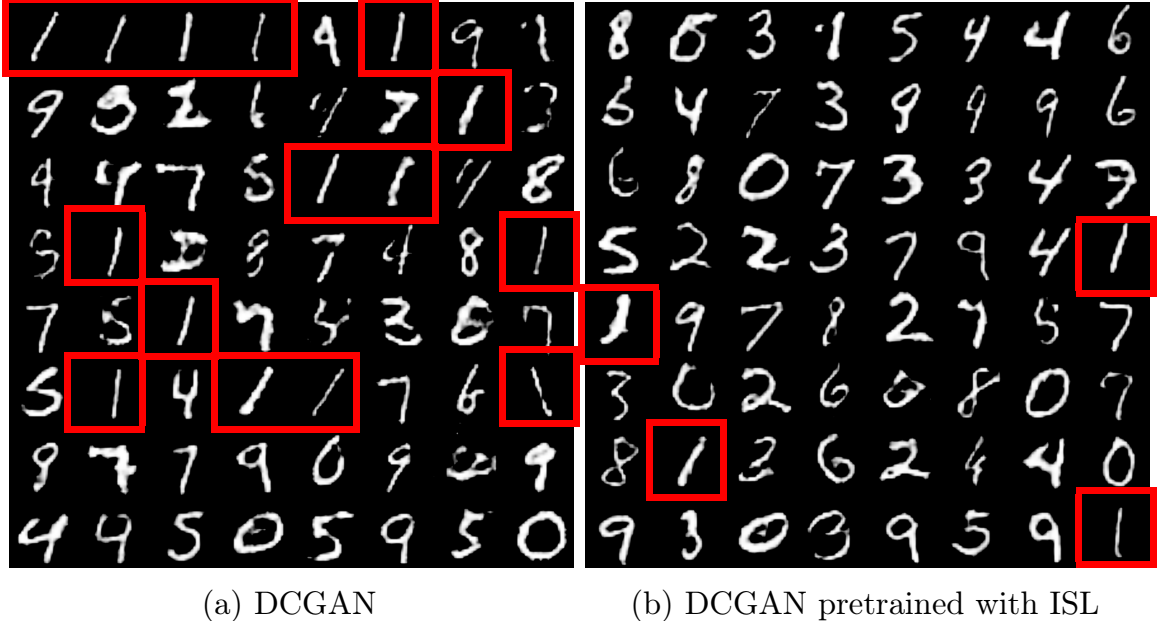


Figure 10: Precision (left) and recall (right) on the MNIST test set after 50 training epochs, using $m = 20$ and $m = 100$ random projections.

Finally, Figure 11 compares the sample diversity of a standard DCGAN Figure 11a against a DCGAN pretrained with our ISL method Figure 11b. In Figure 11a, the red boxes highlight multiple occurrences of the digit “1,” a clear sign of mode collapse where the generator repeatedly produces the same class. After pretraining with ISL (Figure 11b), the generator exhibits far fewer repeated “1”s, instead producing more diverse handwritten digits. This visual evidence demonstrates that ISL pretraining effectively mitigates mode collapse and encourages the generator to cover a broader range of the MNIST data distribution.

4.5 Improving diversity on CelebA with ISL pretraining

In this section, we evaluate ISL pretraining on the CelebA dataset under a unified 50-epoch regime. We first pretrain a DCGAN with ISL for 10 epochs (learning rate 10^2 , $K = 40$), then fine-tune it adversarially for 40 epochs (batch size 128, learning rate 2×10^{-4}). For a fair



(a) DCGAN

(b) DCGAN pretrained with ISL

Figure 11: Generated samples from the MNIST dataset: plot (a) shows numbers generated by a DCGAN, while the plot (b) shows numbers generated by a DCGAN pretrained with ISL. Red squares around the repeated “1”’s.

comparison, we trained every baseline using 50 epochs, batch size 128, and a grid search over learning rates $\{1 \times 10^{-2}, 1 \times 10^{-3}, 2 \times 10^{-4}, 1 \times 10^{-4}\}$. The baselines we evaluated were

- Generative multi-adversarial networks (GMAN) (Durugkar et al., 2016): uses multiple discriminators to improve mode coverage.
- Least-aquares DCGAN (LS-DCGAN) (Mao et al., 2017): swaps the usual cross-entropy loss for a least-squares objective.
- Wasserstein GAN with gradient penalty (W-DCGAN-GP) (Gulrajani et al., 2017): enforces the 1-Lipschitz constraint via a gradient penalty.
- Spectral normalization DCGAN (SN-DCGAN) (Miyato et al., 2018): stabilizes training by normalizing discriminator weights.
- Dynamic GAN (DynGAN) (Luo and Yang, 2024): detects collapsed modes during training and uses conditional generators to recover them.

From each model’s single run, we report the best recall, Fréchet Inception Distance (FID), and precision scores. Full details are provided in Table 8.

Remarkably, our ISL-pretrained DCGAN achieves the highest recall of all models, despite its relative simplicity. It even outperforms multi-discriminator frameworks such as GMAN—while using three times fewer parameters—and specialized techniques like DynGAN, which introduce semi-supervised overhead to recover collapsed modes. Moreover, in terms of both FID and precision, the ISL-pretrained network remains highly competitive, despite

fitted only on 40 adversarial training epochs (10 fewer than every baseline). These results underscore the power of ISL pretraining to capture diverse image modes without extra architectural complexity.

Dataset	Method	<i>FID</i> \downarrow	<i>Precision</i> \uparrow	<i>Recall</i> \uparrow
CelebA	ISL + DCGAN	31.64	0.887	0.954
	DCGAN (Radford et al., 2015)	30.93	0.839	0.834
	LS-DCGAN (Mao et al., 2017)	22.99	0.997	0.324
	W-DCGAN-GP (Gulrajani et al., 2017)	80.30	0.982	0.374
	SN-DCGAN (Miyato et al., 2018)	32.94	0.974	0.887
	DynGAN (Luo and Yang, 2024)	48.06	0.955	0.718
	GMAN (Durugkar et al., 2016)	31.66	0.873	0.888

Table 8: Performance comparison on CelebA. We evaluate ISL-pretrained DCGAN (ISL+DCGAN), standard DCGAN, Least Squares DCGAN (LS-DCGAN), Spectral Normalization DCGAN (SN-DCGAN), DynGAN, and Generative Multi-Adversarial Networks (GMAN) using Fréchet Inception Distance (*FID* \downarrow), precision (\uparrow), and recall (\uparrow). Lower *FID* and higher precision/recall indicate better sample quality and diversity.

Our two-stage training pipeline (first pretraining the generator by minimizing ISL, then fine-tuning it with standard adversarial updates) parallels the strategy of the sliced-Wasserstein generator (SWG) from Nadjahi et al. (2021). In SWG, the authors begin by minimizing a Monte Carlo estimate of the sliced-Wasserstein distance in feature space before introducing a discriminator (see Nadjahi et al. (2021, Sec. 3.2)). They motivate this design by noting that naive slicing in very high dimensions demands an impractically large number of random projections; adding a learned discriminator effectively reduces the problem’s dimensionality to the most discriminative subspace, thereby cutting the projection requirement and restoring strong *FID* performance. We build on exactly this insight: by replacing the Monte Carlo sliced-Wasserstein objective with ISL during the initial phase, we still “warm up” the generator into a space close to the real-data manifold, but with a discrepancy measure that more directly reduces mode collapse. Under identical hyperparameter settings and evaluation protocols, ISL pretraining achieves substantially higher recall on every benchmark, while matching the precision and *FID* of SWG. These results confirm that ISL is a more effective statistical divergence than sliced-Wasserstein for preserving diversity without sacrificing sample fidelity. Table 9 provides the full comparison, highlighting the superior recall of ISL alongside equivalent precision and *FID*.

5 Time series prediction

Our approach applies to both univariate and multivariate time series. Hereafter we briefly describe the methodology for both types for series and conclude the section with experiments comparing these techniques on various datasets.

m	ISL + DCGAN			SWG			SWG-2		
	FID ↓	Precision ↑	Recall ↑	FID ↓	Precision ↑	Recall ↑	FID ↓	Precision ↑	Recall ↑
100	31.64	0.89	0.95	32.82	1.00	0.16	34.57	1.00	0.14
1 000	30.41	0.91	0.94	37.27	0.98	0.68	35.83	1.00	0.56
10 000	30.33	0.92	0.93	37.29	0.98	0.63	37.20	0.99	0.74

Table 9: Comparison for CelebA between ISL + DCGAN, the Sliced-Wasserstein Generator (SWG), and its Sliced-Wasserstein-2 variant (SWG-2) as a function of the number of random projections m . Lower FID and higher precision/recall indicate better sample quality and diversity.

5.1 Univariate time series prediction

Let $y[0], y[1], \dots, y[T]$ represent a realization of a discrete-time random process. We assume that the process begins at $t = 0$, $Y[t]$ denotes the r.v. at time t , and $p_t = p(Y[t]|Y[0], \dots, Y[t-1])$ is the unknown conditional distribution. Given the sequence $y[0], y[1], \dots, y[t-1]$, we aim to train an autoregressive conditional implicit generator network, $g_\theta(z_t, \mathbf{h}[t])$, to approximate p_t . Here, z_t is a sequence of i.i.d. Gaussian r.v.s, and $\mathbf{h}[t]$ is an embedding of the sequence $y[0], \dots, y[t-1]$ via a NN, such as a simple RNN connected to the generator (see Figure 12). At time t , the observation $y[t]$ is fed into the RNN, compressing the history into a hidden state $\mathbf{h}[t]$. The generator $g_\theta(z, \mathbf{h}[t])$ uses this hidden state and noise z to predict $\tilde{y}[t+1]$. During testing, $\tilde{y}[t+1]$ is fed back into the RNN for forecasting.

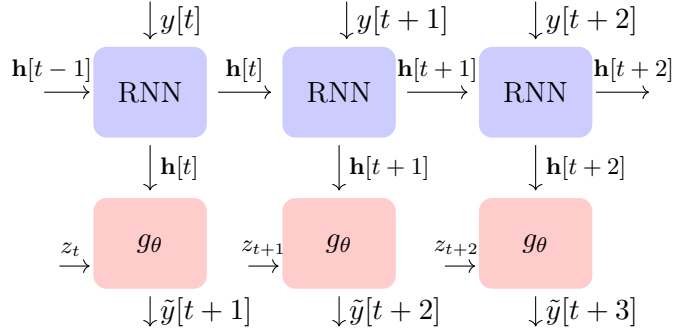


Figure 12: Conditional implicit generative model for time-series prediction.

As noted in de Frutos et al. (2024), all results from previous sections remain valid in this temporal setup. The sequence of observations $\mathbf{y} = [y[0], y[1], \dots, y[T]]$ is used to construct a sequence of statistics $a_K[0], a_K[1], \dots, a_K[T]$, whose empirical distribution should be approximately uniform if $\tilde{p}_{t,\theta} \approx p_t$ for $t = 0, \dots, T$, where $\tilde{p}_{t,\theta}$ is the pdf of the output r.v. $\tilde{y}[t] = g_\theta(z_t, \mathbf{h}[t])$. To build the ISL, we follow the same procedure described in Section 2 to obtain a differentiable surrogate.

5.2 Multivariate time series prediction

For a multivariate time series the data has the form $\mathbf{y} = [\mathbf{y}[0], \dots, \mathbf{y}[T]]$ where each element of the series is an N -dimensional vector, i.e., $\mathbf{y}[t] = [y_1[t], \dots, y_N[t]]^\top$. A NN $g_\theta(\cdot, \mathbf{h}[t])$ can

be trained using the same scheme as in Figure 12 and an ISL loss function constructed from the N marginals $p(y_i[t]|\mathbf{y}[0], \dots, \mathbf{y}[t-1])$, as suggested in de Frutos et al. (2024), or using the ISL-slicing (Algorithm 2) method introduced in Section 4.

5.3 Experiments

This subsection presents the results of multivariate long-sequence time-series forecasting on the ETTh2, ETTm1, and ETTm2 datasets using Autoformer (Wu et al., 2021), Informer (Zhou et al., 2021), LogTrans (Nie et al., 2022) and various ISL-based methods. The Electricity Transformer Temperature (ETT) dataset comprises four distinct subsets: two with hourly resolutions (ETTh) and two with 15-minute resolutions (ETTm), each containing seven features related to oil and load characteristics of electricity transformers collected between July 2016 and July 2018. For more details on the methods and datasets, refer to Zeng et al. (2023). The evaluation spans multiple forecasting horizons (τ) and is assessed using two key metrics: mean squared error (MSE) and mean absolute error (MAE). Detailed results are provided in Table 10.

For these experiments, we use a 1-layer RNN with 5 units, followed by batch normalization and a 2-layer MLP with 10 units per layer. The MLP has ReLU in the first layer, identity activation in the last, and 5% dropout in the first layer. Despite this simple architecture, ISL outperforms state-of-the-art transformers. We also observe that the ISL-slicing method generally performs better than both the marginal fitting technique and other state-of-the-art methods, with improvements as the number of projections increases. Notably, the ISL models (with $\approx 25K$ parameters), using an RNN and a simple MLP, achieves better forecasting accuracy than many transformer models with millions of parameters (Zeng et al., 2023).

DB	τ	Autoformer		Informer		LogTrans		ISL-M		ISL-S7		ISL-S10		ISL-S20	
		MSE	MAE	MSE	MAE	MSE	MAE	MSE	MAE	MSE	MAE	MSE	MAE	MSE	MAE
ETTh2	96	0.36	0.40	3.76	1.53	2.12	1.20	0.42	0.49	0.31	0.45	0.28	0.43	0.26	0.41
	192	0.46	0.45	5.60	1.93	4.32	1.63	0.68	0.69	0.61	0.64	0.54	0.57	0.55	0.60
	336	0.48	0.49	4.72	1.84	1.12	1.60	0.61	0.64	0.41	0.55	0.33	0.43	0.44	0.51
	720	0.52	0.51	3.65	1.63	3.19	1.54	0.60	0.62	0.75	0.68	0.56	0.57	0.65	0.64
ETTm1	96	0.67	0.57	0.54	0.51	0.60	0.55	0.41	0.51	0.43	0.55	0.28	0.43	0.19	0.37
	192	0.80	0.67	0.56	0.54	0.84	0.70	0.57	0.62	0.67	0.65	0.35	0.36	0.30	0.49
	336	1.21	0.87	0.75	0.66	1.12	0.83	0.70	0.67	0.79	0.78	0.67	0.68	0.54	0.61
	720	1.17	0.82	0.91	0.72	1.15	0.82	0.77	0.69	0.92	0.73	0.87	0.77	0.76	0.74
ETTm2	96	0.26	0.34	0.37	0.45	0.77	0.64	0.28	0.44	0.21	0.38	0.22	0.37	0.22	0.36
	192	0.28	0.34	0.53	0.56	0.99	0.76	0.34	0.46	0.33	0.43	0.26	0.40	0.21	0.34
	336	0.34	0.37	1.36	0.89	1.33	0.87	0.31	0.46	0.37	0.47	0.31	0.45	0.15	0.31
	720	0.43	0.43	3.38	1.34	3.05	1.33	0.43	0.55	0.37	0.50	0.36	0.49	0.24	0.40

Table 10: Forecasting results for multivariate time-series on ETTh2, ETTm1, and ETTm2 datasets using Autoformer, Informer, LogTrans and ISL. ISL-M denotes the marginal approach, and ISL-S n is the ISL-slicing with n random projections.

6 Conclusions

We have investigated the construction of loss functions based on rank statistics with an invariant distribution in order to train implicit generative models that can reproduce heavy-tailed and multivariate data distributions. As a result, we have introduced two novel methodologies, Pareto-ISL and ISL-slicing. Pareto-ISL is used to fit a NN with a Pareto-distributed random input. The resulting model can represent accurately both the central features and the tails of heavy-tailed data distributions. ISL-slicing can be used to train NN with a random input and a high-dimensional output. We have shown through simulations with several data sets (including time series data) that the proposed methods are competitive with (and often outperform) state of the art models. The computational cost of training generative models with ISL-based methods is usually low compared to that of state of the art schemes.

Acknowledgments and Disclosure of Funding

This work has been partially supported by the Office of Naval Research (award N00014-22-1-2647) and Spain's Agencia Estatal de Investigación (ref. PID2021-125159NB-I00 TYCHE and PID2021-123182OB-I00 EPiCENTER) funded by MCIN/AEI/10.13039/501100011033 and by "ERDF A way of making Europe". Also funded by Comunidad de Madrid IND2022/TIC-23550, IDEA-CM project (TEC-2024/COM-89) and the ELLIS Unit Madrid (European Laboratory for Learning and Intelligent Systems). Pablo M. Olmos was also supported by the 2024 Leonardo Grant for Scientific Research and Cultural Creation from the BBVA Foundation.

Appendix A. Proof of Theorem 2

Proof For clarity, we introduce the following notation: for a real function $f : \mathbb{R} \rightarrow \mathbb{R}$ and the pdf p of a univariate r.v. we define

$$(f, p) := \int_{\mathbb{R}} f(x)p(x) dx.$$

Let $B_1(\mathbb{R}) := \{f : \mathbb{R} \rightarrow \mathbb{R} \mid \sup_{x \in \mathbb{R}} |f(x)| \leq 1\}$ be the set of real functions bounded by 1. We note that the assumption $\sup_{f \in B_1(\mathbb{R})} |(f, p) - (f, \tilde{p})|$ in (de Frutos et al., 2024, Theorem 2) is equivalent to the assumption of Theorem 4. Indeed,

$$\begin{aligned} \|p - \tilde{p}\|_{L^1(\mathbb{R})} &= \int_{\mathbb{R}} |p(x) - \tilde{p}(x)| dx = \int_{\mathbb{R}} \text{sgn}(p(x) - \tilde{p}(x))(p(x) - \tilde{p}(x)) dx \\ &= \sup_{f \in B_1(\mathbb{R})} |(f, p) - (f, \tilde{p})|. \end{aligned}$$

The remainder of the proof follows directly from (de Frutos et al., 2024, Theorem 2). \blacksquare

Appendix B. Proof of Theorem 4

B.1 Preliminary results

Let, $\tilde{F}_\theta(y_0)$ represents the cdf of the transformed r.v. $y = g_\theta(z)$, evaluated at y_0 , where g_θ is a function parameterized by θ . The r.v. y has a pdf denoted \tilde{p}_θ and $z \sim p_z$.

Let $\tilde{y}_1, \dots, \tilde{y}_K$ be K iid draws from \tilde{p}_θ . Using $\tilde{F}_\theta(y_0)$, we define the probability of observing exactly n successes in K independent Bernoulli trials. The i -th trial is considered a success when $\tilde{y}_i \leq y_0$, hence the success probability is $\tilde{F}_\theta(y_0)$. We write of the resulting binomial distribution as

$$h_{n,\theta}(y_0) = \binom{K}{n} \left[\tilde{F}_\theta(y_0) \right]^n \left[1 - \tilde{F}_\theta(y_0) \right]^{K-n}, \quad \text{for } n \in \{0, \dots, K\}. \quad (\text{B.1})$$

Using B.1, the pmf of the rank statistic $A_K = |\{\tilde{y} \in \{\tilde{y}_i\}_{i=1}^K : \tilde{y} \leq y_0\}|$ when $y_0 \sim \tilde{p}_\theta$ can be constructed as

$$\mathbb{Q}_{K,\tilde{p}_\theta}(n) = \int_{\mathbb{R}} h_{n,\theta}(y) \tilde{p}_\theta(y) dy, \quad \text{for } n \in \{0, \dots, K\}. \quad (\text{B.2})$$

Lemma 1 *The cdf $\tilde{F}_\theta(y_0) = \mathbb{P}(g_\theta(z) \leq y_0)$ is continuous in θ , for every fixed $y_0 \in \mathbb{R}$.*

Proof The cdf $\tilde{F}_\theta(y_0)$ can be expressed as

$$\tilde{F}_\theta(y_0) = \mathbb{P}(y \leq y_0) = \mathbb{P}(g_\theta(z) \leq y_0) = \int_{\mathbb{R}} \mathbb{I}_{S_{y_0,\theta}}(z) p_z(z) dz,$$

where p_z is the pdf of the input noise, $S_{y_0,\theta} = \{u \in \mathbb{R} : g_\theta(u) \leq y_0\}$ and $\mathbb{I}_{S_{y_0,\theta}}(z)$ is the indicator function. We need to prove that for any sequence $\{\theta_m\}_{m=1}^\infty$ such that $\theta_m \rightarrow \theta$ as $m \rightarrow \infty$, we have $\lim_{m \rightarrow \infty} |\tilde{F}_{\theta_m}(y_0) - \tilde{F}_\theta(y_0)| = 0$. We can write

$$|\tilde{F}_{\theta_m}(y_0) - \tilde{F}_\theta(y_0)| \leq \int_{\mathbb{R}} |\mathbb{I}_{S_{y_0,\theta_m}}(z) - \mathbb{I}_{S_{y_0,\theta}}(z)| p_z(z) dz.$$

If we define the set $A_m = \{u \in \mathbb{R} : (g_\theta(u) \leq y_0 < g_{\theta_m}(u)) \text{ or } (g_{\theta_m}(u) \leq y_0 < g_\theta(u))\}$ then is clear that

$$\left| \mathbb{I}_{S_{y_0, \theta_m}}(z) - \mathbb{I}_{S_{y_0, \theta}}(z) \right| = \begin{cases} 1 & \text{if } z \in A_m, \\ 0 & \text{otherwise.} \end{cases}$$

Hence, we can write

$$\left| \tilde{F}_{\theta_m}(y_0) - \tilde{F}_\theta(y_0) \right| = \int_{\mathbb{R}} \mathbb{I}_{A_m}(z) p_z(z) dz = \int_{A_m} p_z(z) dz, \quad (\text{B.3})$$

and there is a constant $C < \infty$ such that $\int_{A_m} p_z(z) dz \leq C \int_{A_m} dz$. However $g_\theta(z)$ is continuous in θ for almost every $z \in \mathbb{R}$, i.e., $\lim_{m \rightarrow \infty} g_{\theta_m}(z) = g_\theta(z)$, which implies that $\lim_{m \rightarrow \infty} \int_{A_m} dz = 0$. Therefore $\lim_{m \rightarrow \infty} \left| \tilde{F}_{\theta_m}(y_0) - \tilde{F}_\theta(y_0) \right| \leq C \int_{A_m} dz = 0$. \blacksquare

Lemma 2 For each $n \in \{0, 1, \dots, K\}$, there is a constant $C_{n,K} < \infty$ such that

$$\left| h_{n,\theta}(y_0) - h_{n,\theta'}(y_0) \right| \leq \binom{K}{n} C_{n,K} \left| \tilde{F}_\theta(y_0) - \tilde{F}_{\theta'}(y_0) \right|.$$

Proof We can bound the difference between $h_{n,\theta}(y_0)$ and $h_{n,\theta'}(y_0)$ using B.1 as

$$\left| h_{n,\theta}(y_0) - h_{n,\theta'}(y_0) \right| \leq \binom{K}{n} \left| \tilde{F}_\theta(y_0)^n (1 - \tilde{F}_\theta(y_0))^{K-n} - \tilde{F}_{\theta'}(y_0)^n (1 - \tilde{F}_{\theta'}(y_0))^{K-n} \right|.$$

Let us define $f(q) = q^n (1 - q)^{K-n}$, which is continuously differentiable for $q \in [0, 1]$. By the mean value theorem, for some value $\tilde{F}_{\theta^*}(y_0) \in [\tilde{F}_\theta(y_0) \wedge \tilde{F}_{\theta'}(y_0), \tilde{F}_\theta(y_0) \vee \tilde{F}_{\theta'}(y_0)]$, we have

$$\left| f(\tilde{F}_\theta(y_0)) - f(\tilde{F}_{\theta'}(y_0)) \right| \leq \left| f'(\tilde{F}_{\theta^*}(y_0)) \right| \left| \tilde{F}_\theta(y_0) - \tilde{F}_{\theta'}(y_0) \right|.$$

Since $f(q) = q^n (1 - q)^{K-n}$ is a polynomial in q , its derivative $f'(q)$ is continuous and bounded on the interval $q \in [0, 1]$. Given that $\tilde{F}_{\theta^*}(y_0) \in [0, 1]$ (as it is a cdf), there exists a constant C_n such that, $\left| f'(\tilde{F}_{\theta^*}(y_0)) \right| \leq C_n$ for any $\tilde{F}_{\theta^*}(y_0)$. \blacksquare

Lemma 3 Let $\tilde{F}_\theta(y_0)$ and $\tilde{F}_{\theta'}(y_0)$ be the cdfs of the transformed r.v.s $y = g_\theta(z)$ and $y' = g_{\theta'}(z)$, respectively, where $g_\theta(z)$ is differentiable w.r.t. z and satisfies the Lipschitz condition $|g_\theta(z) - g_{\theta'}(z)| \leq L_{\max} \|\theta - \theta'\|$ for some Lipschitz constant $L_{\max} < \infty$, and there exists $m > 0$ such that $\inf_{(z,\theta)} |g'_\theta(z)| \geq m$. Then

$$\left| \tilde{F}_\theta(y_0) - \tilde{F}_{\theta'}(y_0) \right| \leq L_1 \|\theta - \theta'\|,$$

where $L_1 = \|p_z\|_{L^\infty(\mathbb{R})} \frac{2L_{\max}}{m}$ and $p_z(z)$ is the pdf of the input variable z .

Proof Let $A = \{u \in \mathbb{R} : (g_\theta(u) \leq y_0 < g_{\theta'}(u)) \text{ or } (g_{\theta'}(u) \leq y_0 < g_\theta(u))\}$. By the same argument as in the proof of Lemma 1 (see Eq. B.3) we have

$$\left| \tilde{F}_\theta(y_0) - \tilde{F}_{\theta'}(y_0) \right| \leq \int_A p_z(z) dz. \quad (\text{B.4})$$

We now prove that $A \subseteq B = \left\{ u \in \mathbb{R} \mid |g_\theta(u) - y_0| \leq L_{\max} \|\theta - \theta'\| \right\}$. For any $z \in A$, there are two possible cases to consider: either $g_\theta(z) \leq y_0 < g_{\theta'}(z)$ or $g_{\theta'}(z) \leq y_0 < g_\theta(z)$. In the first case, we can see that $|g_\theta(z) - y_0| \leq |g_\theta(z) - g_{\theta'}(z)| \leq L_{\max} \|\theta - \theta'\|$ by the Lipschitz assumption. An analogous argument holds for the second case. Thus, we have shown that for any $z \in A$, $|g_\theta(z) - y_0| \leq L_{\max} \|\theta - \theta'\|$ and, therefore, $A \subseteq B$.

Next, we estimate the Lebesgue measure $\mathcal{L}(B)$ of the set B . By assumption, $g_\theta(z)$ is differentiable w.r.t. z , with $\inf_{(z,\theta) \in \mathcal{Z} \times \mathbb{R}^d} |g'_\theta(z)| \geq m > 0$. Hence, we can perform a change of variable $y = g_\theta(z)$, and obtain $z = g_\theta^{-1}(y)$, where g_θ^{-1} is the local inverse function. We note that $z \in B$ when $y \in [y_0 - \delta, y_0 + \delta]$, where $\delta = L_{\max} \|\theta - \theta'\|$. The Lebesgue measure of B can be upper bounded as

$$\mathcal{L}(B) = \int_B dz \leq \int_{y_0 - \delta}^{y_0 + \delta} \left| \frac{dz}{dy} \right| dy \leq \frac{1}{m} \int_{y_0 - \delta}^{y_0 + \delta} dy = \frac{2\delta}{m} = \frac{2L_{\max}}{m} \|\theta - \theta'\|,$$

since $\frac{dz}{dy} = \frac{1}{g'_\theta(z)}$ and, by assumption, $\inf_{(z,\theta)} |g'_\theta(z)| \geq m$, hence $\left| \frac{dz}{dy} \right| = \frac{1}{|g'_\theta(z)|} \leq \frac{1}{m}$.

Finally, we proceed to bound the absolute difference between the cdfs. In particular,

$$\left| \tilde{F}_\theta(y_0) - \tilde{F}_{\theta'}(y_0) \right| \leq \int_A p_z(z) dz \leq \int_B p_z(z) dz \leq \|p_z\|_{L^\infty(\mathbb{R})} \mathcal{L}(B) \leq L_1 \|\theta - \theta'\|,$$

the first inequality follows from B.4, the second is given by $A \subseteq B$, and the last inequality follow from the upper bound on $\mathcal{L}(B)$ with $L_1 = \|p_z\|_{L^\infty(\mathbb{R})} \frac{2L_{\max}}{m}$. \blacksquare

B.2 Proof of Theorem 4

Proof Continuity (Part 1)

To prove that $d_K(p, \tilde{p}_\theta)$ is continuous w.r.t. θ , we need to show that

$$\lim_{m \rightarrow \infty} |d_K(p, \tilde{p}_{\theta_m}) - d_K(p, \tilde{p}_\theta)| = 0$$

for any sequence $\{\theta_m\}_{m=1}^\infty$ such that $\theta_m \rightarrow \theta$.

We begin by examining the difference $|d_K(p, \tilde{p}_{\theta_m}) - d_K(p, \tilde{p}_\theta)|$. Let us denote $\mathbf{q}_{K, \tilde{p}_\theta} = [\mathbb{Q}_{K, \tilde{p}_\theta}(0), \dots, \mathbb{Q}_{K, \tilde{p}_\theta}(K)]^\top$. We readily arrive at the bound

$$\begin{aligned} |d_K(p, \tilde{p}_{\theta_m}) - d_K(p, \tilde{p}_\theta)| &= \frac{1}{K+1} \left| \left\| \frac{1}{K+1} \mathbf{1}_{K+1} - \mathbf{q}_{K, \tilde{p}_{\theta_m}} \right\|_{\ell_1} - \left\| \frac{1}{K+1} \mathbf{1}_{K+1} - \mathbf{q}_{K, \tilde{p}_\theta} \right\|_{\ell_1} \right| \\ &\leq \frac{1}{K+1} \|\mathbf{q}_{K, \tilde{p}_{\theta_m}} - \mathbf{q}_{K, \tilde{p}_\theta}\|_{\ell_1} \end{aligned} \quad (\text{B.5})$$

$$\leq \frac{1}{K+1} \sum_{n=0}^K \int_{\mathbb{R}} |h_{n, \theta_m}(y) - h_{n, \theta}(y)| \max\{\tilde{p}_{\theta_m}(y), \tilde{p}_\theta(y)\} dy, \quad (\text{B.6})$$

where (B.5) follows from the reverse triangle inequality and (B.6) is obtained from the construction of the pmf $\mathbb{Q}_{K, \tilde{p}_\theta}(n)$ in Eq. (B.2). It is easy to see that

$$|h_{n, \theta_m}(y) - h_{n, \theta}(y)| \max\{\tilde{p}_{\theta_m}(y), \tilde{p}_\theta(y)\} \leq 2(\tilde{p}_\theta(y) + \tilde{p}_{\theta_m}(y)),$$

hence the dominated convergence theorem yields

$$\lim_{m \rightarrow \infty} |d_K(p, \tilde{p}_{\theta_m}) - d_K(p, \tilde{p}_\theta)| \leq \sum_{n=0}^K \int_{\mathbb{R}} \lim_{m \rightarrow \infty} |h_{n, \theta_m}(y) - h_{n, \theta}(y)| \max\{\tilde{p}_{\theta_m}(y), \tilde{p}_\theta(y)\} dy. \quad (\text{B.7})$$

However, $h_{n, \theta_m}(y)$ is continuous in θ because it depends continuously on the cdf $\tilde{F}_{\theta_m}(y)$ which, in turn, is continuous by Lemma 1. Therefore,

$$\lim_{m \rightarrow \infty} |h_{n, \theta_m}(y) - h_{n, \theta}(y)| = 0 \quad (\text{B.8})$$

for any sequence $\{\theta_m\}_{m=1}^\infty$ such that $\theta_m \rightarrow \theta$. Combining (B.8) with the inequality (B.7) yields $\lim_{m \rightarrow \infty} |d_K(p, \tilde{p}_{\theta_m}) - d_K(p, \tilde{p}_\theta)| = 0$ whenever $\theta_m \rightarrow \theta$ and completes the proof of Part 1. \blacksquare

Proof Differentiability (Part 2).

By Rademacher's theorem (see (Evans, 2018, Theorem 3.2)), if $d_K(p, \tilde{p}_\theta)$ is Lipschitz then it is differentiable almost everywhere. Hence, we aim to prove that $d_K(p, \tilde{p}_\theta)$ is Lipschitz continuous w.r.t. θ .

Lemma 2 yields the upper bound

$$|h_{n, \theta}(y_0) - h_{n, \theta'}(y_0)| \leq \binom{K}{n} C_{n, K} |\tilde{F}_\theta(y_0) - \tilde{F}_{\theta'}(y_0)|, \quad (\text{B.9})$$

where $C_{n, K} < \infty$ is a constant that depends on n and K . Combining (B.9) with Lemma 3 yields the Lipschitz continuity of $h_{n, \theta}(y_0)$, namely

$$|h_{n, \theta}(y_0) - h_{n, \theta'}(y_0)| \leq \binom{K}{n} C_{n, K} L_1 \|\theta - \theta'\|, \quad (\text{B.10})$$

where $L_1 < \infty$ is a constant. Moreover, we have a bound for the pdf \tilde{p}_θ of the form

$$\sup_{\theta, y} \tilde{p}_\theta(y) = \sup_{\theta, y} \frac{p_z(g_\theta^{-1}(y))}{|g'_\theta(g_\theta^{-1}(y))|} \leq \frac{\|p_z\|_{L^\infty(\mathbb{R})}}{m}, \quad (\text{B.11})$$

where $g_\theta^{-1}(y)$ is the local inverse of $g_\theta(y)$ and we have used the assumption $\inf_{z, \theta} |g'_\theta(z)| \geq m > 0$. Substituting the upper bounds (B.10) and (B.11) back into (B.6) (with $\theta_m = \theta'$) yields

$$|d_K(p, \tilde{p}_\theta) - d_K(p, \tilde{p}_{\theta'})| \leq \frac{1}{K+1} \frac{\|p_z\|_{L^\infty(\mathbb{R})}}{m} \sum_{n=0}^K \binom{K}{n} C_{n, K} L_1 \|\theta - \theta'\|.$$

Finally, we note that $\sum_{n=0}^K \binom{K}{n} = 2^K$ to obtain

$$|d_K(p, \tilde{p}_\theta) - d_K(p, \tilde{p}_{\theta'})| \leq \frac{\|p_z\|_{L^\infty(\mathbb{R})}}{m(K+1)} 2^K \left(\max_{0 \leq n \leq K} C_{n, K} \right) L_1 \|\theta - \theta'\|.$$

and complete the proof. ■

Appendix C. Experimental results

C.1 Comparison of the surrogate and theoretical loss functions

Table 11 compares the error rates between the surrogate and theoretical losses. The metrics displayed include the L_1 and L_∞ norms of the values obtained from the surrogate loss and the theoretical loss at each epoch, along with their respective percentage errors. In this setup the noise is drawn from a standard Gaussian, $\mathcal{N}(0, 1)$, the number of training epochs is 1000, $K = 10$, the sample size is $N = 1000$, and the results are averaged over 100 trials. The final three rows in the table describe mixture models with equal component weights: Model 1 is a mixture of $\mathcal{N}(5, 2)$ and $\mathcal{N}(-1, 1)$, Model 2 is a mixture of $\mathcal{N}(5, 2)$, $\mathcal{N}(-1, 1)$, and $\mathcal{N}(-10, 3)$, and Model 3 is a mixture of $\mathcal{N}(-5, 2)$ and Pareto(5, 1).

Target	L_1	L_∞	% error L_1	% error L_∞
$\mathcal{N}(4, 2)$	0.005307 \pm 0.001505	0.254805 \pm 0.034452	0.019625	0.930903
$\mathcal{U}(-2, 2)$	0.015454 \pm 0.001450	0.244568 \pm 0.028237	0.015454	0.734944
Cauchy(1,2)	0.005192 \pm 0.001329	0.242361 \pm 0.028494	0.015636	0.729832
Pareto(1,1)	0.003290 \pm 0.004527	0.137377 \pm 0.183803	0.000547	0.022837
Model ₁	0.004701 \pm 0.002198	0.175290 \pm 0.025778	0.003925	1.471159
Model ₂	0.004991 \pm 0.001895	0.173241 \pm 0.030297	0.033870	0.117551
Model ₃	0.009817 \pm 0.002167	0.348440 \pm 0.068293	0.016706	0.592932

Table 11: Comparison of error between the surrogate and theoretical losses. Noise is $\sim \mathcal{N}(0, 1)$, $K = 10$, epochs = 1000, and $N = 1000$. Entries are mean \pm std over 100 trials; last two columns show percentage error.

Figure 13 illustrates the surrogate loss versus the theoretical one across several distributions, presented in log-scale to highlight performance differences.

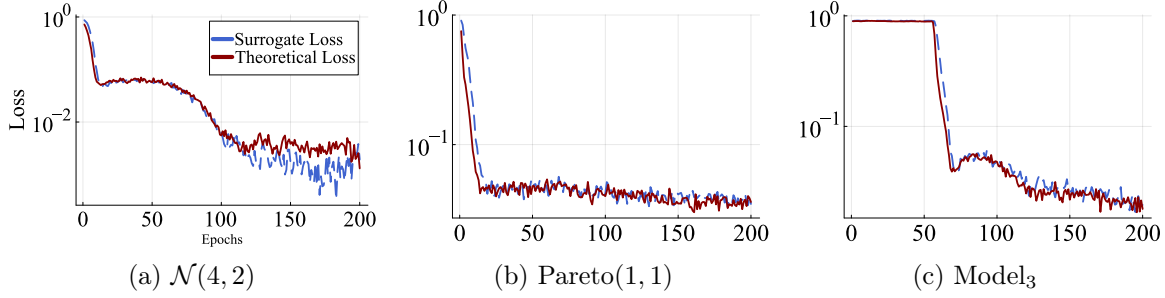


Figure 13: Comparison of the surrogate loss and the theoretical one during training for different distributions. Only the first 200 epochs are shown, and the scale in the vertical axis is logarithmic.

In conclusion, the surrogate loss performs well for different target distributions, as shown in Table 11 and Figure 13. The small L_1 and L_∞ norms with minimal percentage errors indicate its close approximation of the theoretical loss. Even for complex distributions like the mixture models, it maintains low error rates, demonstrating robustness and reliability.

C.2 Efficiency gains from progressive K training vs. fixed K

In Table 12, we compare the outcomes of progressively increasing K during training against a fixed K value. After running 100 trials and averaging the results, we found that progressively increasing K reduces training time by up to 50% without sacrificing accuracy. Additionally, the KSD values are comparable or slightly better, indicating that this strategy offers a more efficient balance between time savings and model performance.

	Progressive K		$K = 10$		Time Imp. %	
	KSD	Time	KSD	Time	Time	
$\mathcal{N}(4, 2)$	0.00831 ± 0.00268	4149	0.00894 ± 0.00276	9016	53.98	
$\mathcal{U}(-2, 2)$	0.01431 ± 0.00158	8721	0.01373 ± 0.00152	11745	25.74	
Cauchy(1,2)	0.01084 ± 0.00146	3700	0.01190 ± 0.00161	8002	53.76	
Pareto(1,1)	0.08344 ± 0.00334	4978	0.24238 ± 0.17257	10800	53.90	
Model ₁	0.01001 ± 0.00134	8000	0.01175 ± 0.00336	11044	27.56	
Model ₂	0.01067 ± 0.00270	11042	0.00921 ± 0.00187	8039	27.19	
Model ₃	0.18525 ± 0.00406	8700	0.18053 ± 0.04512	11207	22.37	

Table 12: Comparison of progressive- K training versus fixed $K = 10$. Noise is $\sim \mathcal{N}(0, 1)$, $K_{\max} = 10$ (progressive only), epochs = 200, and $N = 1000$. Times are in seconds; “KSD” entries are mean \pm std.

C.3 Comparing ISL and Pareto-ISL for approximating heavy-tailed multi-dimensional distributions

We define multidimensional distributions with heavy-tailed characteristics and train a generator to approximate them. Specifically, we introduce a joint distribution on $[X_0, X_1]$ with the following component definitions

$$X_0 = A + B, \quad X_1 = \text{sign}(A - B) |A - B|^{1/2},$$

where A and B are independent Cauchy r.vs. with location 0.5 and scale 1.0. Note that X_0 and X_1 have different tail indices (1 and 1/2, respectively) and are not independent.

We trained a Pareto-ISL model on this distribution using a NN with an input layer of 2 features, followed by three hidden layers of 256 neurons each with ReLU activations. The input was a mixture of GPD with tail indices of 1 and 0.5. As shown in Figure 14, the marginals and joint distributions closely match the target. We also compared these results to those obtained using ISL with multivariate normal input noise, characterized by a zero mean and identity covariance matrix.

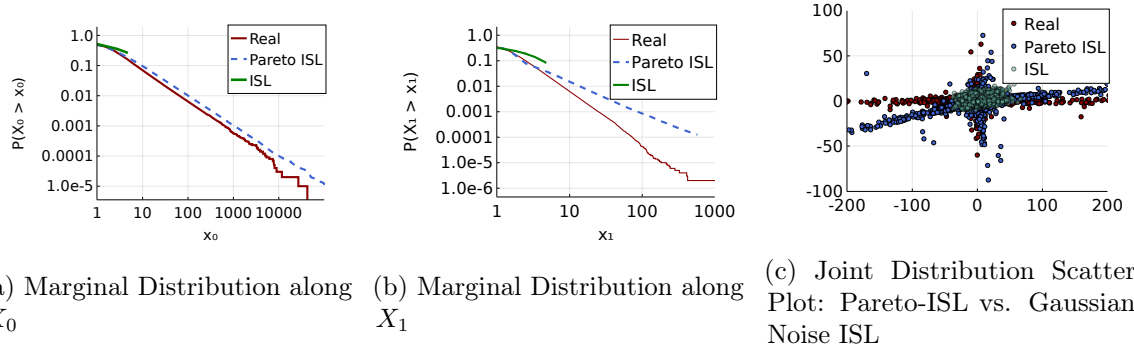


Figure 14: Plots (a) and (b) show the marginal distributions along the X_0 and X_1 axes for the Pareto-ISL model and ISL with Gaussian noise. Plot (c) presents a scatter plot of 10000 samples from both models, illustrating the joint distribution between the two dimensions.

Appendix D. Experimental Setup

All experiments were performed on a MacBook Pro running macOS 13.2.1, equipped with an Apple M1 Pro CPU and 16 GB of RAM. When GPU acceleration was required, we used a single NVIDIA TITAN Xp with 12 GB of VRAM. Detailed hyperparameter settings for each experiment are provided in the corresponding sections.

References

Martin Arjovsky, Soumith Chintala, and Léon Bottou. Wasserstein generative adversarial networks. In *International conference on machine learning*, pages 214–223. PMLR, 2017.

Raman Arora, Amitabh Basu, Poorya Mianjy, and Anirbit Mukherjee. Understanding deep neural networks with rectified linear units. *arXiv preprint arXiv:1611.01491*, 2016.

Sanjeev Arora, Rong Ge, Yingyu Liang, Tengyu Ma, and Yi Zhang. Towards principled methods for training generative adversarial networks. In *International Conference on Learning Representations (ICLR)*, 2018.

August A Balkema and Laurens De Haan. Residual life time at great age. *The Annals of probability*, 2(5):792–804, 1974.

Marc G Bellemare, Ivo Danihelka, Will Dabney, Shakir Mohamed, Balaji Lakshminarayanan, Stephan Hoyer, and Rémi Munos. The cramer distance as a solution to biased wasserstein gradients. *arXiv preprint arXiv:1705.10743*, 2017.

Siddharth Bhatia, Arjit Jain, and Bryan Hooi. Exgan: Adversarial generation of extreme samples. In *Proceedings of the AAAI Conference on Artificial Intelligence*, volume 35, pages 6750–6758, 2021.

Nicolas Bonneel, Julien Rabin, Gabriel Peyré, and Hanspeter Pfister. Sliced and radon wasserstein barycenters of measures. *Journal of Mathematical Imaging and Vision*, 51: 22–45, 2015.

Haim Brézis. *Functional analysis, Sobolev spaces and partial differential equations*, volume 2. Springer, 2011.

Andrew Brock, Jeff Donahue, and Karen Simonyan. Large scale gan training for high fidelity natural image synthesis. *arXiv preprint arXiv:1809.11096*, 2018.

Xi Chen, Yan Duan, Rein Houthooft, John Schulman, Ilya Sutskever, and Pieter Abbeel. Infogan: Interpretable representation learning by information maximizing generative adversarial nets. *Advances in neural information processing systems*, 29, 2016.

Ziyu Chen, Markos Katsoulakis, Luc Rey-Bellet, and Wei Zhu. Sample complexity of probability divergences under group symmetry. In *International Conference on Machine Learning*, pages 4713–4734. PMLR, 2023.

Jinyoung Choi and Bohyung Han. Mcl-gan: Generative adversarial networks with multiple specialized discriminators. *Advances in Neural Information Processing Systems*, 35:29597–29609, 2022.

Stuart Coles, Joanna Bawa, Lesley Trenner, and Pat Dorazio. *An introduction to statistical modeling of extreme values*, volume 208. Springer, 2001.

José Manuel de Frutos, Pablo Olmos, Manuel A. Vázquez, and Joaquín Míguez. Training implicit generative models via an invariant statistical loss. In *International Conference on Artificial Intelligence and Statistics*, pages 2026–2034. PMLR, 2024.

Laurent Dinh, Jascha Sohl-Dickstein, and Samy Bengio. Density estimation using real nvp. *arXiv preprint arXiv:1605.08803*, 2016.

Petar M Djuric and Joaquín Míguez. Assessment of nonlinear dynamic models by kolmogorov–smirnov statistics. *IEEE transactions on signal processing*, 58(10):5069–5079, 2010.

Ishan Durugkar, Ian Gemp, and Sridhar Mahadevan. Generative multi-adversarial networks. *arXiv preprint arXiv:1611.01673*, 2016.

Víctor Elvira, Joaquín Miguez, and Petar M Djurić. On the performance of particle filters with adaptive number of particles. *Statistics and Computing*, 31:1–18, 2021.

LawrenceCraig Evans. *Measure theory and fine properties of functions*. Routledge, 2018.

Yanxiang Gong, Zhiwei Xie, Mei Xie, and Xin Ma. Testing generated distributions in gans to penalize mode collapse. In *International Conference on Artificial Intelligence and Statistics*, pages 442–450. PMLR, 2024.

Ian Goodfellow, Jean Pouget-Abadie, Mehdi Mirza, Bing Xu, David Warde-Farley, Sherjil Ozair, Aaron Courville, and Yoshua Bengio. Generative adversarial nets. *Advances in neural information processing systems*, 27, 2014.

Alexander N Gorban and Ivan Yu Tyukin. Blessing of dimensionality: mathematical foundations of the statistical physics of data. *Philosophical Transactions of the Royal Society A: Mathematical, Physical and Engineering Sciences*, 376(2118):20170237, 2018.

Ishaan Gulrajani, Faruk Ahmed, Martin Arjovsky, Vincent Dumoulin, and Aaron C Courville. Improved training of wasserstein gans. *Advances in neural information processing systems*, 30, 2017.

Jonathan Ho, Ajay Jain, and Pieter Abbeel. Denoising diffusion probabilistic models. *Advances in neural information processing systems*, 33:6840–6851, 2020.

Todd Huster, Jeremy Cohen, Zinan Lin, Kevin Chan, Charles Kamhoua, Nandi O Leslie, Cho-Yu Jason Chiang, and Vyas Sekar. Pareto gan: Extending the representational power of gans to heavy-tailed distributions. In *International Conference on Machine Learning*, pages 4523–4532. PMLR, 2021.

Tero Karras, Samuli Laine, and Timo Aila. A style-based generator architecture for generative adversarial networks. In *Proceedings of the IEEE/CVF conference on computer vision and pattern recognition*, pages 4401–4410, 2019.

Tero Karras, Samuli Laine, Miika Aittala, Janne Hellsten, Jaakko Lehtinen, and Timo Aila. Analyzing and improving the image quality of stylegan. In *Proceedings of the IEEE/CVF conference on computer vision and pattern recognition*, pages 8110–8119, 2020.

Tero Karras, Miika Aittala, Samuli Laine, Erik Härkönen, Janne Hellsten, Jaakko Lehtinen, and Timo Aila. Alias-free generative adversarial networks. *Advances in neural information processing systems*, 34:852–863, 2021.

Diederik P Kingma, Max Welling, et al. Auto-encoding variational bayes, 2013.

Soheil Kolouri, Kimia Nadjahi, Umut Simsekli, Roland Badeau, and Gustavo Rohde. Generalized sliced wasserstein distances. *Advances in neural information processing systems*, 32, 2019.

Chun-Liang Li, Wei-Cheng Chang, Yu Cheng, Yiming Yang, and Barnabás Póczos. MMD GAN: Towards deeper understanding of moment matching network. *Advances in neural information processing systems*, 30, 2017.

Haoye Lu, Yiwei Lu, Dihong Jiang, Spencer Ryan Szabados, Sun Sun, and Yaoliang Yu. Cm-gan: Stabilizing gan training with consistency models. In *ICML 2023 Workshop on Structured Probabilistic Inference \& Generative Modeling*, 2023.

Yixin Luo and Zhouwang Yang. Dyngan: Solving mode collapse in GANs with dynamic clustering. *IEEE Transactions on Pattern Analysis and Machine Intelligence*, 2024.

Xudong Mao, Qing Li, Haoran Xie, Raymond YK Lau, Zhen Wang, and Stephen Paul Smolley. Least squares generative adversarial networks. In *Proceedings of the IEEE international conference on computer vision*, pages 2794–2802, 2017.

L Markovich. Light-and heavy-tailed density estimation by gamma-weibull kernel. In *Conference of the International Society for Non-Parametric Statistics*, pages 145–158. Springer, 2016.

Lars Mescheder, Andreas Geiger, and Sebastian Nowozin. Which training methods for gans do actually converge? In *International conference on machine learning*, pages 3481–3490. PMLR, 2018.

Luke Metz, Ben Poole, David Pfau, and Jascha Sohl-Dickstein. Unrolled generative adversarial networks. *arXiv preprint arXiv:1611.02163*, 2016.

Takeru Miyato, Toshiki Kataoka, Masanori Koyama, and Yuichi Yoshida. Spectral normalization for generative adversarial networks. *arXiv preprint arXiv:1802.05957*, 2018.

Shakir Mohamed and Balaji Lakshminarayanan. Learning in implicit generative models. *arXiv preprint arXiv:1610.03483*, 2016.

Kimia Nadjahi, Alain Durmus, Pierre E Jacob, Roland Badeau, and Umut Simsekli. Fast approximation of the sliced-wasserstein distance using concentration of random projections. *Advances in Neural Information Processing Systems*, 34:12411–12424, 2021.

Xingqing Nie, Xiaogen Zhou, Zhiqiang Li, Luoyan Wang, Xingtao Lin, and Tong Tong. Logtrans: Providing efficient local-global fusion with transformer and cnn parallel network for biomedical image segmentation. In *2022 IEEE 24th Int Conf on High Performance Computing & Communications; 8th Int Conf on Data Science & Systems; 20th Int Conf on Smart City; 8th Int Conf on Dependability in Sensor, Cloud & Big Data Systems & Application (HPCC/DSS/SmartCity/DependSys)*, pages 769–776. IEEE, 2022.

George Papamakarios, Eric Nalisnick, Danilo Jimenez Rezende, Shakir Mohamed, and Balaji Lakshminarayanan. Normalizing flows for probabilistic modeling and inference. *Journal of Machine Learning Research*, 22(57):1–64, 2021.

Alec Radford, Luke Metz, and Soumith Chintala. Unsupervised representation learning with deep convolutional generative adversarial networks. *arXiv preprint arXiv:1511.06434*, 2015.

Sidney Resnick and Cătălin Stărică. Smoothing the hill estimator. *Advances in Applied Probability*, 29(1):271–293, 1997.

Murray Rosenblatt. Remarks on a multivariate transformation. *The annals of mathematical statistics*, 23(3):470–472, 1952.

Yunus Saatci and Andrew G Wilson. Bayesian gan. *Advances in neural information processing systems*, 30, 2017.

Mehdi SM Sajjadi, Olivier Bachem, Mario Lucic, Olivier Bousquet, and Sylvain Gelly. Assessing generative models via precision and recall. *Advances in neural information processing systems*, 31, 2018.

Jangwon Seo, Hyo-Seok Hwang, Minhyeok Lee, and Junhee Seok. Stabilized gan models training with kernel-histogram transformation and probability mass function distance. *Applied Soft Computing*, 164:112003, 2024.

Connor Shorten and Taghi M Khoshgoftaar. A survey on image data augmentation for deep learning. *Journal of big data*, 6(1):1–48, 2019.

Akash Srivastava, Lazar Valkov, Chris Russell, Michael U Gutmann, and Charles Sutton. Veegan: Reducing mode collapse in GANs using implicit variational learning. *Advances in neural information processing systems*, 30, 2017.

Vincent Stimper, David Liu, Andrew Campbell, Vincent Berenz, Lukas Ryll, Bernhard Schölkopf, and José Miguel Hernández-Lobato. normflows: A pytorch package for normalizing flows. *Journal of Open Source Software*, 8(86):5361, 2023. doi: 10.21105/joss.05361. URL <https://doi.org/10.21105/joss.05361>.

Masashi Sugiyama, Song Liu, Marthinus Christoffel du Plessis, Masao Yamanaka, Makoto Yamada, Taiji Suzuki, and Takafumi Kanamori. Direct divergence approximation between probability distributions and its applications in machine learning. *Journal of Computing Science and Engineering*, 7(2):99–111, 2013.

Haixu Wu, Jiehui Xu, Jianmin Wang, and Mingsheng Long. Autoformer: Decomposition transformers with auto-correlation for long-term series forecasting. *Advances in Neural Information Processing Systems*, 34:22419–22430, 2021.

Chang Xiao, Peilin Zhong, and Changxi Zheng. Bourgan: Generative networks with metric embeddings. *Advances in neural information processing systems*, 31, 2018.

Ailing Zeng, Muxi Chen, Lei Zhang, and Qiang Xu. Are transformers effective for time series forecasting? In *Proceedings of the AAAI conference on artificial intelligence*, volume 37, pages 11121–11128, 2023.

Peilin Zhong, Yuchen Mo, Chang Xiao, Pengyu Chen, and Changxi Zheng. Rethinking generative mode coverage: A pointwise guaranteed approach. *Advances in Neural Information Processing Systems*, 32, 2019.

Haoyi Zhou, Shanghang Zhang, Jieqi Peng, Shuai Zhang, Jianxin Li, Hui Xiong, and Wancai Zhang. Informer: Beyond efficient transformer for long sequence time-series forecasting. In *Proceedings of the AAAI conference on artificial intelligence*, volume 35, pages 11106–11115, 2021.